

Sparse Algorithms for EEG Source Localization

Teja Mannepalli, Aurobinda Routray

the date of receipt and acceptance should be inserted later

Abstract Source localization using EEG is important in diagnosing various physiological and psychiatric diseases related to the brain. The high temporal resolution of EEG helps medical professionals to assess the internal physiology of the brain in a more informative way. The internal sources are obtained from EEG by an inversion process. The number of sources in the brain outnumber the number of measurements. In this article, a comprehensive review of the state-of-the-art sparse source localization methods in this field is presented. A recently developed method, certainty-based-reduced-sparse-solution (CARSS) is implemented and is examined. A vast comparative study is performed using a sixty-four channel setup involving two source spaces. The first source space has 5,004 sources and the other has 2,004 sources. Four test cases with one, three, five, and seven simulated active source (s) are considered. Two noise levels are also being added to the noiseless data. The CARSS is also evaluated. The results are examined. A real EEG study is also attempted.

Keywords Electroencephalograph · Ill-posed problem · Source localization · Sparse signal reconstruction.

1 Introduction

The study of physiological and neurophysiological aspects of the brain is important to diagnose the health of the brain. For this, two techniques are available- radiological and electro-magnetic. Radiological techniques like fMRI, CT that are although non-invasive, involve radiological emissions. It can accurately provide the internal anatomy of the brain. This is used for studying structural anomalies. However, the low temporal resolution does not recommend these methods to analyze the behavioral symptoms of the brain. Therefore, the EEG and MEG have been accepted as the de facto standards for studying behavioral syndromes like epilepsy and sleep disorders. Over the years, effective numerical computing tools have been made available by the researchers for carrying out the inversion processes by way of which surface measurements could be mapped to the internal sources of the cortex. The high time-resolution of EEG combined with the inversion provides the opportunity to analyze the brain-behavior in more detail (Sanei and Chambers [2013]) (Michel et al. [2009]) (Murray et al. [2008])(Michel and Murray [2012]).

1.1 EEG source localization

The EEG source localization is the inversion of surface measurements and mapping to the internal sources of the cortex (Grech et al. [2008]). This helps to study and understand brain activity at a better temporal resolution. The sources in the brain outnumber the number of measurements. This results in an ill-posed problem. The source distribution is not sparse at any point in time. The source activity is oscillatory. How-

T. Mannepalli
Indian Institute of Technology, Kharagpur, India. PIN: 721 302
Tel.: +91 96 35 88 5811
E-mail: mteja134@gmail.com

A. Routray
Indian Institute of Technology, Kharagpur, India. PIN: 721 302
E-mail: aurobinda.routray@gmail.com

ever, in an experimental setting (like during capture of any event-related potential - ERP) in which many trials can be averaged, the non-task-related activity cancels out. An event-related potential (ERP) is the measured brain response that results in specific sensory, cognitive, or motor event. The problem is treated as a linear model implying a linear combination between EEG measurements and sources. The fact is derived from the linearity of Maxwell's equations of the measurements and sources. The localization of unknown active sources from the known EEG measurements is the *inverse problem*. The linear operator, lead field matrix predicts the electromagnetic fields generated due to an array of sources by the EEG channels. Two main types of approaches are commonly used to solve this problem:

1. The parametric or dipole fitting approach. They assume limited dipoles are responsible for explaining the measurements. The location and orientation of the dipoles are unknown.
2. The non-parametric approach or distributed source model. Several dipoles are distributed uniformly all over the brain. The current article deals with this approach.

1.2 Neurological origin of problem

The neural activations produce electro-magnetic fields in the brain. The human brain contains hundreds of billions of neurons. Some millions of neurons collectively and synchronously fire with a potential in the same orientation resulting in a post-synaptic potential (PSP). The PSP is of the magnitude of about 10 mV with a duration of 10 ms. They will be emerging as a measurable potential on the scalp. EEG measures the collective activity of the neurons.

Most potentials originate from pyramidal cells. Grey matter is dominated by neuronal cell bodies and synapses and relatively few myelinated axons. They are the 'generators' of the potential. White matter is dominated by the myelinated axons and has relatively few cell bodies. They are the 'transmitters' of the potential. (Friston [2008]) (Baillet et al. [2001]). The sources of EEG are the current generators. They are modeled as current dipoles.

1.3 Need and importance of the source localization

The EEG along with source localization is effectively used to analyze a wide range of disorders such as Alzheimer's disease, epilepsy, seizures, tumors, and brain anomalies (Nolte and Sundsten [2009]) (Sanei and

Chambers [2013]). The complex brain pathways under several cognitive as well as emotional tasks can also be studied effectively (Nolte and Sundsten [2009]). Many medical professionals claim EEG as a valuable tool due to its high temporal resolution. This helps to study the brain in detail.

1.4 Challenges in Source Localization

The primary challenge is ill-posedness. Further, the solution has to be unambiguous. The head and brain models need to comply with anatomical and structural constraints of the brain. The data from fMRI can be used for this (Oostenveld et al. [2011]). The process of acquiring pure EEG signals from raw data requires advanced pre-processing techniques and strategies. The generalization of the cortical information across all the subjects is not generally allowed by the medical community. However, such a generalized model can be used to get an overview of internal brain activity.

1.5 Overview of the current manuscript

The current manuscript deals with the problem of source localization using EEG. The manuscript is organized as follows. Background deals with the problem definition, characteristics of the problem, and solution strategy. The literature review deals with the current state of art techniques. The next section deals with the challenges posed by this problem and the setbacks of the methods. Five methods are implemented and are compared. The methods are again solved with reduced solution space by a newly developed method by the authors namely certainty-based reduced sparse solution (CARSS) ((Mannepalli and Routray [2019])). A real data study is evaluated.

2 Background

2.1 Problem definition

The distributed source models involve inversion of the lead field matrix. The distribution of the current generators in practice is defined over a discrete set of locations. The current dipoles are positioned in the cortex (Dale and Sereno [1993]). The source estimates are simply the amplitudes of the dipoles. The distribution is scalar-valued when only their amplitudes are not known. It will be vector-valued if the amplitudes and orientations are unknown. The sources can be either defined over a surface or a volume. The surface-based

source models distribute the dipoles over the cortex. The approach involves the 2D surface of the cortex and is first proposed by (Dale and Sereno [1993]). The other way is to sample the dipoles on a regular 3D grid in the cortex.

First, the cortex is sectioned into small 3D volumes called voxels. Each voxel is assumed as a source and is assigned a dipole. The distributed source model has a known dipole location with an unknown dipole moment (Grech et al. [2008]). This has been posed as a problem of sparse signal reconstruction from limited data measurements in the context of an ERP study. The problem has two properties (1) sources outnumbering the measurements. (2) few active sources among many at a particular time instant (Sanei and Chambers [2013]). The distributed source problem is formulated as:

$$\mathbf{Y} = \mathbf{K}\mathbf{X} + \mathbf{E} \quad (1)$$

\mathbf{Y} is the measurement vector of size $N \times T$ and \mathbf{K} is the forward matrix (or also known as lead field matrix) (Hallez et al. [2007]), (Grech et al. [2008]). N is the number of electrodes on the scalp, and M is the number of voxels. Each voxel is assigned a dipole or three dipoles orthogonal to each other. The degrees of freedom of a source can be considered three (dipoles having 'free' orientations) or one (dipoles having 'fixed' orientations). More on the interpretation of the lead field matrix is clarified in Section - 2.3. \mathbf{X} is the magnitude of unknown weights of sources with size $3M \times T$. \mathbf{E} is the noise. The essence of the inverse problem boils down to minimizing the cost function \mathbf{F} :

$$\mathbf{F} = \arg \min_{\mathbf{X}} \frac{1}{2} \|\mathbf{Y} - \mathbf{K}\mathbf{X}\|_a^2 + f(\mathbf{X}) \quad (2)$$

The loss function evaluates the sources active from the measurement vector taking care of the noise. Ideally, the minimization of the loss function is equivalent to computing a maximum likelihood estimate under the assumption of Gaussian noise. In reality, a noise covariance matrix needs to be estimated as the noise will not be Gaussian exactly. The regularization parameter α controls the trade-off between the accuracy in the measurements and the noise sensitivity. Also to note, the weights for each of the columns of the lead field matrix need to be incorporated. This is to counterbalance the deep sources. It can be obtained by normalization of each column of \mathbf{K} . This is a common way to address this issue. The $f(\mathbf{X})$ is the penalty or regularization term. It introduces an *a priori* knowledge of the solution. Penalization is required to obtain a unique solution. To obtain a globally optimum solution, the

$\|\mathbf{Y}(\tau) - \mathbf{K}\mathbf{X}(\tau)\|_a^2$ and $f(\mathbf{X}(\tau))$ need to be convex functions.

2.2 Problem Characteristics

1. *Ill-posedness*: It is a well-known fact that the number of unknown sources outnumber the number of measurements at any point in time (Sanei and Chambers [2013]). This leads to a case of an under-determined inversion problem having multiple solutions and hence ill-posedness.
2. *Spatiotemporal Sparsity*: The source distribution is not sparse at any time. However, many trials are averaged in an experimental setting (ERP experiments), so that any non-task-related activity cancels (Grech et al. [2008]). The sources are considered sparse concerning space and time during an ERP. The spatial sparsity is justified only for the experimental setting. Also, the evidence from other neuroimaging techniques, such as fMRI and ECoG has revealed the compact nature of cortical activations. The sources are *locally clustered* and *globally sparse*.
3. *Depth bias*: The shallow sources have a greater effect on the scalp electrodes as compared to the deep sources due to internal attenuation (Hallez et al. [2007]). The effect needs to be weighed against the depth. The naive inverse problem will favor the shallow sources.
4. *Spatial correlation*: The neighboring sources in the cortex are synchronized with each other at any moment (Grech et al. [2008]). This ensures the continuity of the ionic current in the neuron. Also, to note, the uneven cortex surface (having gyrus and sulcus) plays an important role in deciding the continuity of the current field among sources (Baillet et al. [2001]).
5. *Temporal correlation/ Common Sparsity*: The sources obey the common sparsity (CSP) assumption subject to a temporal neighborhood (Zhang and Rao [2011]) (Friston [2008]) (Michel et al. [2004]). A source is estimated to maintain the CSP for 10-20 ms (Zhang and Rao [2011]).
6. *Anatomical Constraints*: There are primarily two anatomical constraints of the problem widely followed (Baillet and Garnero [1997] (Baillet et al. [2001]). They are:
 - (a) **Fixed orientations**: The orientations of the dipoles are believed to be primarily dominated by the ones perpendicular to the cortical surface (Baillet and Garnero [1997]) (Baillet et al. [2001]). This is because the dipoles activating upwards cannot be canceled by other dipoles.

This reduces the orientations of the dipole from three to one. Some researchers, however, still consider the orientations of the dipole as three.

- (b) **Location of the dipoles:** The sources will be present predominantly in the grey matter and limited in the white (Nunez et al. [2006]) (Dale and Sereno [1993]) (Haufe et al. [2013]).
7. *Physiological constraints:* Some of the physiological constraints subject to the present problem are:
- (a) **Smoothness:** The sampling frequency of EEG is in general considered more than adequate for capturing the temporal neuronal activity of the sources. This assures the smoothness of the dipole magnitudes (Dale and Sereno [1993]) (Baillet et al. [2001]).
- (b) **Functional dependency of cortical patches:** The cortex is known not to be a smooth surface. The structural complexity of the cortex decides the functional dependency between patches. In some cases, the adjacent patches can be functionally independent (Baillet and Garnero [1997]).
8. *Non-stationarity of the sources:* While the CSP characteristic is valid for some time, the non-stationarity of sources cannot be eluded. The sources are not stationary with time. The instantaneous solvers generally ignore this fact (Gramfort et al. [2013]), (Friston et al. [2008]).
9. *Characteristics of noise:* During an evoked response study, the 'noise' is the signal from the brain from non-targeted stimuli. This is known as 'baseline noise'. In the case of MEG, the noise co-variances can be estimated using 'empty room' recordings. There are two ways for which noise covariance is estimated- one is the 'resting baseline' and the other is the 'pre-stimulation baseline' (Baillet et al. [2001]). The EEG is recorded for the subjects in the resting state. The noise covariance is estimated from these segments of data. The procedure is the 'resting baseline'. The noise-covariance matrix allows the weight of the channels correctly and estimates the noise covariances of each. The noise-covariance matrix provides information about the field and potential patterns representing uninteresting noise sources.

2.3 Solution strategy

Before solving the problem of source localization in a distributed model source scenario, a framework of the data has to be followed. A broad schematic of the methodology followed is presented in Fig. 1.

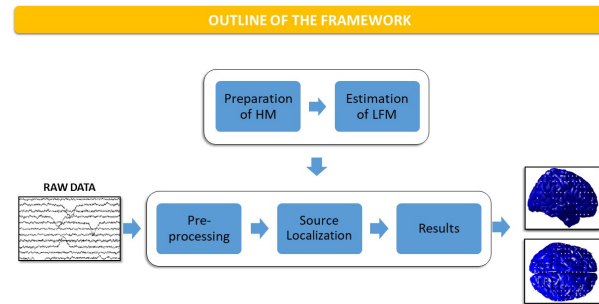


Fig. 1 The outline of the approach followed in general. HM: Head model; LFM: lead field matrix

2.3.1 Pre-processing

The raw data is pre-processed to remove noise and artifacts. The artifacts are of two origins- physiological and non-physiological. The artifacts of physiological origin are due to head movements, eye blinks, heartbeat, muscle artifacts, etc. The artifacts of non-physiological origin can be added due to line frequency, cable defects, electronic noises, etc. The artifacts have to be observed and removed carefully. More on the pre-processing of EEG can be found in (Sanei and Chambers [2013]).

2.3.2 Preparation of the head model

The head, skull, and brain models with appropriate measurements are designed. An MRI is converted to the brain model by using a toolbox like Fieldtrip (Oostenveld et al. [2011]) or Brainstorm (Baillet et al. [2001]) (Mosher et al. [2005]) or MNE (Gramfort et al. [2014]) etc.

2.3.3 Estimation of the lead field matrix

The dipoles are distributed over the source space. There exist two approaches to prepare a head-model - surface-based approach or volume-based approach. The source space can be defined as a volume or as a surface. The following procedure adequately fits the volume-based approach. The dipoles are distributed on a regular 2D or 3D grid with needed inter-grid sample distance m within the cortex. A dipole is considered to have either a 'fixed' orientation or 'free' orientation. The orientation of the dipole is fixed perpendicular to the cortical sheet. If then the dipoles have a 'fixed' orientation. If the orientation is left unconstrained, three orthogonal dipoles are placed along the cartesian ' x ',

'y,' and 'z' directions (Gonçalves et al. [2003]) (Hallez et al. [2007]) (Gonçalves et al. [2003]) (Hallez et al. [2007]).

Lead field matrix: The potential due to a dipole at i^{th} electrode on the scalp is $\mathbf{k}_j^i = V(\mathbf{r}_{scalp,i}, \mathbf{r}_{dipole,j}, \mathbf{d})$; $i = 1 \dots N$; $j = 1 \dots M$. $\mathbf{r}_{scalp,i}$ is the position of i^{th} electrode on the scalp. $\mathbf{r}_{dipole,j}$ is the j^{th} source location in the brain. $\mathbf{d} = d_j \mathbf{e}_j$ is the dipole moment with magnitude $d_j = [d_{j,x}, d_{j,y}, d_{j,z}]$ and orientation $\mathbf{e}_j = \frac{\mathbf{d}_j}{\|\mathbf{d}_j\|}$. Each dipole with three orientations results in three column vectors $\mathbf{k}_j = [k_{j,x}; k_{j,y}; k_{j,z}]$. Each column vector $k_{j,x}$ is of size $N \times 1$. All the column vectors are arranged to frame the lead field matrix

$$\mathbf{K} = \begin{bmatrix} k_{1,x}^1 & k_{1,y}^1 & k_{1,z}^1 & k_{2,x}^1 & k_{2,y}^1 & k_{2,z}^1 & \dots & k_{M,x}^1 & k_{M,y}^1 & k_{M,z}^1 \\ k_{1,x}^2 & k_{1,y}^2 & k_{1,z}^2 & k_{2,x}^2 & k_{2,y}^2 & k_{2,z}^2 & \dots & k_{M,x}^2 & k_{M,y}^2 & k_{M,z}^2 \\ \vdots & \dots & \vdots & & & & & & & \\ k_{1,x}^N & k_{1,y}^N & k_{1,z}^N & k_{2,x}^N & k_{2,y}^N & k_{2,z}^N & \dots & k_{M,x}^N & k_{M,y}^N & k_{M,z}^N \end{bmatrix} \quad (3)$$

of size $N \times 3M$. \mathbf{K} contains the information regarding the sources. The lead field matrix \mathbf{K} as in Eq. 1 is computed using three concentric sphere models or the boundary element method, or finite element method, or finite difference method, etc. according to the choice (Hallez et al. [2007]).

3 Literature Review

The current section is organized into four sub-sections. They are instantaneous solvers, time-block solvers, Bayesian-based learning solvers, tensor-based solvers, and extended source solvers. The instantaneous solvers solve the problem (as in Eq. 1) instant by instant independent of each other. They employ vector-based norms to minimize the cost function in Eq. 2.

3.1 Instantaneous solvers with non-sparse priors

If the orientations of the sources are free, both the amplitudes and orientations of the current sources need to be estimated. The linear problem to be solved turns out to be:

$$\mathbf{Y} = \mathbf{KX} + \mathbf{E} \quad (4)$$

\mathbf{Y} is the measurement vector of size $N \times 1$. \mathbf{K} is the lead field matrix of size $N \times 3M$ and \mathbf{X} has unknown

source amplitudes and orientations. \mathbf{E} is noise. The Lagrangian estimate \mathbf{X}^* of the true source distribution is given by the solution to the optimization problem:

$$\mathbf{X}^* = \arg \min_{\mathbf{X}} \frac{1}{2} \|\mathbf{Y} - \mathbf{KX}\|_{fro}^2, \text{ subject to } \|\mathbf{X}\| \leq \epsilon \quad (5)$$

The norm denoted by *fro* corresponds to the Frobenius norm of the matrix and the parameter ϵ controls the regularity of the solution. The first part of the equation $\|\mathbf{Y} - \mathbf{KX}\|_{fro}$ is the reconstruction error. The $\|\mathbf{X}\| \leq \epsilon$ means imposing the solution to be small for the Frobenius norm.

Any other norm other than the Frobenius norm can be used in this method. In this regard, there can be many 'minimum norm solvers' in the EEG community, the minimum-norm solution usually only refers to the minimization of an ℓ_2 norm (Gramfort [2009]). The ℓ_1 priors become non-differentiable constraints and cannot be cast as this Lagrangian formulation and derive the solution that easily.

On deriving the differentiable and unconstrained problem in Eq. 5,

$$F = \arg \min_{\mathbf{X}} \frac{1}{2} \|\mathbf{Y} - \mathbf{KX}\|_{fro}^2 + \alpha \|\mathbf{X}\| \quad (6)$$

Using Woodbury matrix identity, the solution will be:

$$\mathbf{X} = \mathbf{TY}, \mathbf{T} = \mathbf{K}^T [\mathbf{K}\mathbf{K}^T + \alpha \mathbf{I}]^\dagger \quad (7)$$

\mathbf{T} is the resolution matrix.

Regularization constant: The regularizing parameter α is estimated using standard regularization techniques like Tikhonov regularization. The Brainstorm toolbox developed an efficient technique to estimate a reasonable α . By replacing \mathbf{K} with its singular value decomposition (SVD) estimate \mathbf{USV}^T in 7, we get

$$\mathbf{X}^* = \mathbf{K}^T \mathbf{U} (\mathbf{S}^2 + \alpha \mathbf{I})^{-1} \mathbf{U}^T \mathbf{Y} \quad (8)$$

The diagonal entries of \mathbf{S} are the singular values $s_{i,i}$ of \mathbf{K} . The singular values are arranged in decreasing order. The matrix $(\mathbf{S}^2 + \alpha \mathbf{I})^{-1}$ is a diagonal matrix with diagonal elements $(s_i^2 + \alpha)$. The α obviously should take a value comparable to the $(s_i^2)_i$. The α is analytically first set as $0.01 s_1^2$.

A few other commonly known methods for estimating α are L-curve and generalized cross-validation (GCV) (Grech et al. [2008]). The L-curve gives the α at the knee point in the log-plot of the solution $\|\mathbf{X}\|$ v/s residual $\|\mathbf{Y} - \mathbf{KX}\|$.

The sLORETA (Pascual-Marqui et al. [2002]) solves the problem using an ℓ_2 norm. The loss function is minimized and is regularized using the ℓ_2 norm. The solution is:

$$\mathbf{X} = \mathbf{T}\mathbf{Y} \text{ where as } \mathbf{T} = \mathbf{K}^T\mathbf{H}[\mathbf{H}\mathbf{K}\mathbf{K}^T\mathbf{H} + \alpha\mathbf{H}]^\dagger \quad (9)$$

sLORETA assumes that the variability in the estimate is due to the sources. \mathbf{H} is the centering matrix. It is equivalent to an average reference operator. The purpose of \mathbf{H} is to normalize the lead field matrix \mathbf{K} . \mathbf{T} is the resolution matrix. The ℓ_2 norm cannot provide the sparsity in the solution. The ℓ_2 norm helps to evenly spread the energy over all the sources. It fails to recover high spatial frequencies. (Gramfort et al. [2012]). The ℓ_2 is less robust to noise compared to the absolute sum ℓ_1 norm. However, it has found successful and simpler to implement (Pascual-Marqui et al. [2002]) (Pascual-Marqui et al. [1994]).

The generalized form of MNE to understand the variants in it is:

$$\mathbf{X} = \mathbf{T}\mathbf{Y}, \mathbf{T} = \mathbf{W}^{-1}\mathbf{K}^T[\mathbf{K}\mathbf{W}^{-1}\mathbf{K}^T + \alpha\mathbf{I}]^\dagger \quad (10)$$

\mathbf{W} is the weight matrix. The characteristics like 'depth bias' are incorporated in \mathbf{W} . \dagger represents pseudo inverse. The minimum norm estimate (MNE) (Dale and Sereno [1993]) (Hämäläinen and Ilmoniemi [1984]) solves the problem by applying the simple identity operator ($\mathbf{W} = \mathbf{I}$). The weighted minimum norm estimate (WMNE) (Grech et al. [2008]) solves the problem by weighting the deep sources ($\mathbf{W} = \text{diag}(\|\mathbf{K}_i\|^2)$, \mathbf{K}_i is the i^{th} column of \mathbf{K}). The low resolution impedance tomography (LORETA) (Pascual-Marqui et al. [1994]) solves by employing a discrete spatial Laplacian operator ($\mathbf{W} = \mathbf{B}\text{diag}(\|\mathbf{K}_i^2\|)$). The method incorporates two factors- the depth of sources and neighborhood correlation of sources.

3.2 Instantaneous solvers with sparse priors

The ℓ_2 norm prior is a non-sparse one although it is differentiable and simple to solve. The main issue with minimum norm solvers is their tendency to smear out the estimated current densities. The solutions delivered will be often quite widespread.

The instantaneous solvers employing sparse priors need to employ an $\ell_{p,p} < 2$ norm as the prior. The $\ell_{p,p} < 2$ norm has a non-linear combinatorial characteristic unlike ℓ_2 norm. The ℓ_0 ideally is supposed to provide the most accurate and sparse solution. However, it is not possible to solve due to the combinatorial

explosion. The $\ell_{p,p} < 2$ norm is used to penalize (or regularize) the solution in (Xu et al. [2007]) (Ou et al. [2009]) to overcome the issues raised by ℓ_2 norm priors. The $\ell_{p,p} < 2$ norm methods need to employ non-linear solvers.

$$\mathbf{F} = \arg \min_x \frac{1}{2} \|\mathbf{Y} - \mathbf{K}\mathbf{X}\|_2^2 + \alpha(\|\mathbf{X}\|_p) \quad (11)$$

The $\ell_{p,p} < 2$ is employed to regularize the solution. The $\ell_{p,p} \geq 1$ is convex and $\ell_{p,p} > 1$ is strictly convex. This makes the respective solvers yield a unique solution.

The conventional minimum ℓ_1 norm solvers suffer from a poor reconstruction of the smoothness of the source activity over time. The implication is given by the ℓ_1 norm solvers from a source activity being substantially a "spiky" one or discontinuous. However, it is not "spiky" rather continuous and oscillatory. The ℓ_1 norm solvers are severely limited by this.

Iterative Recursive System solvers (ITERS): The basic idea of an ITER, as the name suggests, solves the problem with the same rule iteratively. ITERs aim to produce a sparse solution. A few common ITERs are minimum current estimate (MCE) and focally under-determined system solver (FOCUSS). Both solve the problem instant by instant. MCE employ the ℓ_1 norm penalization (Matsuura and Okabe [1995]). FOCUSS uses an ℓ_2 norm reweighted scheme to approximate the ℓ_0 norm regularized method (Gorodnitsky et al. [1995]) (Gorodnitsky and Rao [1997]). It tries to involve similar to ℓ_0 norm penalization. The cost function the FOCUSS solver employs is:

$$\mathbf{x}^* = \arg \min_x \frac{1}{2} \|\mathbf{y} - \mathbf{K}\mathbf{x}\|_2^2 + \|\mathbf{x}\|_0 \quad (12)$$

\mathbf{y} is $N \times 1$ measurement vector and \mathbf{x} is the $M \times 1$ source vector. The FOCUSS solves the problem in Eq. 1 employing inversion with its past solution iteratively.

$$\mathbf{C}_i = \text{diag}([\mathbf{X}_{i-1}(1) \dots \mathbf{X}_{i-1}(3M)]) \quad (13)$$

$$\mathbf{q}_i = (\mathbf{K}\mathbf{C}_i)^\dagger \mathbf{Y} \quad (14)$$

$$\mathbf{X}_i = \mathbf{C}_i \mathbf{q}_i \text{ until converges} \quad (15)$$

\mathbf{C}_i is the weight factor depending on $(i-1)^{\text{th}}$ or past solution. The solver weights its past solution and tries to converge.

Issues with ITERS: ITERS are known to give sparse results. However, the convergence to the local minima instead of the global occurs in many cases (Wipf [2006]). Adding to this, the ITERS is largely dependent on the initial solution and is highly sensitive to noise. The major issue is the scattering of the solution.

3.3 Time block solvers

The instantaneous solvers employ vector norms to penalize the solution whereas the time block solvers employ mixed norms like the ℓ_{21} (Gramfort et al. [2012]). While the above solvers deliver a sparse solution, they fail to recover the time profile of the sources. The time-block solvers enable us to collectively analyze the cortex in space and time domains jointly. There are many novel works performed in this domain in recent times that aim to bring out a joint space time-frequency approach (Strohmeier et al. [2016]).

Two-level mixed norms : Let $\mathbf{x} \in R^P$ be a sequence indexed by a paired indexes (g, m) . The two indices are the hierarchy of the coefficients. g means 'group' index and m mean 'membership' index. The idea behind this is that the coefficients within the same group (indexed by g as $(x_{g,1}, x_{g,2} \dots)$) are *correlated* and coefficients that are distinguished between the groups are *uncorrelated* with each other. Let p, q be the sequence of strictly positive values ≥ 1 . Let \mathbf{w} be weights. The mixed norm of \mathbf{x} is defined as:

$$\|\mathbf{x}\|_{p,q} = \sum_g \left(\sum_m (w_{g,m} |x_{g,m}|^p)^{\frac{q}{p}} \right)^{\frac{1}{q}} \quad (16)$$

By employing a mixed norm, a linkup between ℓ_1 and ℓ_2 norms is obtained. Using this the temporal dynamics in the data can be precisely inferred. The cost function for any mixed norm estimate (MxNE) solver is:

$$\mathbf{X}^* = \arg \min_{\mathbf{X}} \left(\frac{1}{2} \|\mathbf{Y} - \mathbf{KX}\|_2^2 + \alpha f(\mathbf{X}) \right) \quad (17)$$

The mixed norm estimate (MxNE - (Gramfort et al. [2012])) utilizes ℓ_{pq} , (p, q be the sequence of strictly positive values ≥ 1) as a before penalizing the solution (Gramfort et al. [2012]) (Gramfort [2009]) (Strohmeier et al. [2016]). The cost function is:

$$\mathbf{F} = \arg \min_{\mathbf{X}} \frac{1}{2} \|\mathbf{Y} - \mathbf{KX}\|_2^2 + \alpha \|\mathbf{X}\|_{21} \quad (18)$$

α is the regularization parameter. The cost function is non-linear and convex. The cost function is solved by proximal gradient methods. They are the extensions of the gradient-based methods used for the optimization of the ℓ_2 norm functions.

This ℓ_{21} norm can deal with space and time factors simultaneously. The ℓ_{21} of \mathbf{X} norm makes a whole group set to zero. If a group is non-zero, all the coefficients in the group will be set to zero. This leads to a row-structured sparsity. It involves sparsity due to the ℓ_1

norm and gradient in the solution due to the ℓ_2 . The ℓ_{21} norm certainly forms a more general class of priors. The work (Gramfort et al. [2012]) also reports the use of a three-level ℓ_{212} norm with space-time and experimental conditions.

The work performed in (Strohmeier et al. [2016]) reports an efficient approach named iterative reweighted Mixed Norm Estimate (irMxNE). It employs a Frobenius norm to minimize the loss function and a quasi-static $\ell_{0.5}$ norm to penalize the solution. The quasi-static $\ell_{0.5}$ norm makes the cost function a non-convex one. To solve a non-convex function, an approach named block coordinate descent (BCD) is proposed. Also to note, the proposed block coordinate descent (BCD) techniques lead to a faster computation than the fast iterative shrinkage algorithms.

In extension to the mixed norm estimate (MxNE), time-frequency mixed norm estimates (TF-MxNE) proposed in (Gramfort et al. [2013]) utilize $\ell_{21} + \ell_1$ norms. The $\ell_{21} + \ell_1$ norm provides scattered row structures. The method works on the assumption that the time course of each dipole is a linear combination of a few Gabor atoms.

$$\mathbf{Y} = \mathbf{KX} + \mathbf{E} = \mathbf{K}\xi\rho + \mathbf{E} \quad (19)$$

The source matrix is decomposed into the Gabor dictionary of atoms as $\mathbf{KJ} = \mathbf{K}\xi\rho$. ρ is the dictionary of G Gabor atoms of size $G \times T$. ξ has the coefficients of the Gabor decomposition with size $M \times G$. The penalization is accomplished by $\ell_{21} + \ell_1$ norm as $\alpha f(\xi) = \alpha_{space} \|\xi\|_{21} + \alpha_{time} \|\xi\|_1$, The cost function to be minimized is:

$$\xi^* = \arg \min_{\xi} \frac{1}{2} \|\mathbf{Y} - \mathbf{K}\xi\rho\|_{fro}^2 + \alpha \Omega(\xi) \quad (20)$$

$\alpha \geq 0$ is the penalizing parameter. If $\Omega(\xi) = \|\xi\|_1$, it corresponds to LASSO problem (Tibshirani et al. [2005]). The ℓ_1 norm does not impose a row structure on source amplitudes. If $\Omega(\xi) = \|\xi\|_{21}$, it corresponds to MxNE problem (Gramfort et al. [2012]). The ℓ_{21} prior on ξ does not produce denoised time series as it does not involve any decomposition. The TF-MxNE employ $\Omega(\xi) = \alpha_{space} \|\xi\|_{21} + \alpha_{time} \|\xi\|_1$. If α_{space} is large, it will lead to a sparse solution spatially. If α_{time} is large, it will lead to a smooth time series.

The main aim of the usage of the Gabor dictionary is to retain the time components (or time spectrum) along with frequency. This in turn helps to understand the non-stationarity of the signal. The $\ell_{21} + \ell_1$ provides the row sparse structure and also simultaneously promoting the sparsity of the decomposition.

The $\ell_1 - \ell_2$ norm-based Spatio-temporal solver proposed in (Ou et al. [2009]) too utilizes the mixed norm ℓ_{12} like the MxNE. They are similar estimators but use different algorithms and approaches to solve. The resulting convex SOCP is solved by interior-point methods. This solver uses ℓ_1 norm in the spatial domain and ℓ_2 norm in the time domain to solve. The bias is estimated by using SVD of \mathbf{Y} . They employ SVD as a temporal basis function.

temporal basis function: The need for temporal basis function is to reconstruct the oscillatory and continuous source activity with good accuracy. It thereby avoids source activity being manifested as discontinuous and "spiky-kind-of" by conventional $\ell_p, p < 1$ norm solvers. To avoid this discontinuity, averaging of the time courses across adjacent sites is performed. However, it reduces the spatial resolution in return. There exists broadly two kinds of approaches to avoid discontinuous source reconstructions. One is building a prior that explicitly incorporates temporal constraint in the cost function as a regularizer (Baillet et al. [2001]). They links-up between the present current estimate and the past.

The other different route is by employing temporal basis functions. VESTAL (Huang et al. [2006]) projects the ℓ_1 norm solutions into a signal subspace defined by a set of temporal basis functions. The SVD of the measurement vector \mathbf{Y} as \mathbf{USV}^T means the linear combinations of vectors in $\mathbf{V}^T = [\mathbf{V}_{(1:\nu)}, \mathbf{V}_{(\nu:N)}]$ represents the time activity about the measurements. The subspace having dominant singular vectors $\mathbf{V}_{\nu:N}$ are chosen. The criterion of choosing the 'dominant' vectors are the ones with χ^2 values in a certain range after every time point. The χ^2 test reflects that the subspace is not 'over-fitted' or 'under fitted'. The same subspace $\mathbf{V}_{\nu:N}$ that explains the time activity of the measurements should explain the same for sources.

The ℓ_1 norm estimates are employed in (Huang et al. [2006]). The ℓ_{21} norm estimate is employed in (Ou et al. [2009]). In Ou et al. [2009], the selection of subspace is such that the S largest SVD components of \mathbf{Y} should "adequately" fits the \mathbf{Y} . The variable S is relatively fixed and is chosen appropriately to the best of the knowledge of sources. The purpose of the use of the data-adaptive temporal basis function specifically is to (1) compactly represent the data which reduces the computation, (2) bypass the difficulties related to the experimental setting (They are high variations in the source activity, too many experimental tasks, and subject-subject variations).

3.4 Learning based methods

There exist many novel works using Bayesian strategies utilizing temporal characteristics. The typical maximum a posteriori solvers with Gaussian likelihood lead to convex optimization problems. The minimum norm methods assume a predefined covariance matrix for the sources. The learning-based methods estimate the prior based on the data. The learning based methods involve estimating the posterior distribution $p(\mathbf{X}|\mathbf{Y})$ incorporating a prior distribution $p(\mathbf{X})$ on the sources and the likelihood function $p(\mathbf{Y}|\mathbf{X})$. The Bayesian representation of Eq. 2 is:

$$p(\mathbf{X}|\mathbf{Y}) = p(\mathbf{X})p(\mathbf{Y}|\mathbf{X}) \quad (21)$$

Learning the prior means learning the source covariance matrix $\Sigma_{\mathbf{X}}$. The source matrix \mathbf{X} and error \mathbf{E} are assumed Gaussian with mean and covariance $N(0, \Sigma_{\mathbf{X}})$ and $N(0, \Sigma_{\mathbf{E}})$. If $\Sigma_{\mathbf{X}}$ and $\Sigma_{\mathbf{E}}$ are known, the \mathbf{X} can be found out using the cost function:

$$\begin{aligned} \mathbf{X}^* &= \arg \min_{\mathbf{X}} \|\mathbf{Y} - \mathbf{KX}\|_{\Sigma_{\mathbf{E}}}^2 + \|\mathbf{X}\|_{\Sigma_{\mathbf{X}}}^2 \\ &= \arg \min_{\mathbf{X}} (\mathbf{Y} - \mathbf{KX})^T \Sigma_{\mathbf{E}}^{-1} (\mathbf{Y} - \mathbf{KX}) + \mathbf{X}^T \Sigma_{\mathbf{X}}^{-1} \mathbf{X} \end{aligned} \quad (22)$$

$\|\mathbf{X}\|_{\Sigma_{\mathbf{X}}} = \text{trace}(\mathbf{X}^T \Sigma_{\mathbf{X}}^{-1} \mathbf{X})$. The solution is $\mathbf{X}^* = \Sigma_{\mathbf{X}} \mathbf{K}^T (\mathbf{KXK}^T + \Sigma_{\mathbf{E}})^{-1} \mathbf{Y}$. If $\Sigma_{\mathbf{X}} = \mathbf{I}$ and $\Sigma_{\mathbf{E}} = \lambda \mathbf{I}$, the solution looks similar to minimum-norm.

The ℓ_2 norm is the prior here. Learning the ℓ_2 norm means learning the source covariance matrix $\Sigma_{\mathbf{E}}$. If the noise covariance matrix $\Sigma_{\mathbf{E}}$ too along with the source covariance matrix $\Sigma_{\mathbf{X}}$ are not known, they are *not* fixed a priori. Then the parameters define a *model*. The $p(\mathbf{Y}|\mathbf{X})$ is called *likelihood*, $p(\mathbf{X}|\mathbf{Y})$ is called *posterior*, $p(\mathbf{X})$ is the prior, and $p(\mathbf{Y})$ is the *model evidence*. In this perspective, the loss function is the likelihood function $p(\mathbf{Y}|\mathbf{X})$ and the sparsity constraint is incorporated as the prior distribution $p(\mathbf{X})$.

The approaches use maximization of the model *evidence*. However, the differences the approaches have are the ways in learning the priors. The concept of model evidence approaches to estimate the source statistics is first performed by (Friston [2008]), (Friston et al. [2008]), and (Friston et al. [2002]) a.k.a Restricted Maximum Likelihood (ReML). ReML estimates hidden variables (hyperparameters) with an iterative procedure that amounts to Expectation-Maximization update rules. As a procedure in the EM rule, ReML involves maximizing a non-convex likelihood function.

The current problem in Eq. 2 can be seen in two ways (1) single measurement vector (SMV),

and (2) multiple measurement vector (MMV). The concept of MMV, in general, is that the non-sparse entries in every column in \mathbf{X} will be identical. The Eq. 2 is re-written as by letting $\iota = \text{vec}(\mathbf{X}) = [X_{11}; \dots; X_{1M}; \dots; X_{L1}; \dots; X_{LM}]$ of size $ML \times 1$, $\mathbf{D} = \mathbf{K} \otimes \mathbf{I}_L$ and $\mathbf{y} = \text{vec}(Y)$ of size $NL \times 1$. vec represents vectorization of a matrix. The \mathbf{I}_N is the identity matrix:

$$\mathbf{y} = \mathbf{K}\iota + \nu$$

$$\mathbf{y} = \sum_{i=1}^N (\mathbf{k}_i \otimes \mathbf{I}_L) \mathbf{x}_i$$

\mathbf{k}_i is the i^{th} column of \mathbf{K} . \otimes represent Kronecker product. This is the 'block sparsity' model.

The sparse Bayesian learning methods are proposed in (Wipf [2006]), (Wipf and Rao [2007]), (Wipf and Nagarajan [2009]), (Wipf et al. [2011]), (Zhang et al. [2008]), (Zhang and Rao [2011]), (Zhang and Rao [2013]) and (Cotter et al. [2005]). It is abbreviated as bSBL. They are volume-based approaches. They select among a high number of priors that fit the data. The model selection induces the sparsity in the cost function. It is done by maximizing a Gaussian approximation of the evidence. The approach is also known as 'type II maximization'. Let the sources $\mathbf{X}_i, i = 1 \dots M$ be mutually independent with Gaussian probability density function

$$p(\mathbf{X}_i, \gamma_i, \mathbf{B}_i) \sim N(0, \gamma_i, \mathbf{B}_i) \quad (23)$$

$$p(\mathbf{Y}|\Sigma_{\mathbf{Y}}) = \int p(\mathbf{Y}|\mathbf{X}p(\mathbf{X}|\Sigma_{\mathbf{Y}})d\mathbf{X} = N(0, \Sigma_{\mathbf{Y}}) \quad (24)$$

This is equivalent to minimizing the negative log maximum likelihood:

$$L = -\log p(\mathbf{Y}|\Sigma_{\mathbf{E}}) = -T \log(|\Sigma_{\mathbf{Y}}|) + \text{trace}(\mathbf{Y}^T \Sigma_{\mathbf{X}} \mathbf{Y}) \quad (25)$$

The measurement covariance matrix $\Sigma_{\mathbf{Y}}$ turns out to be:

$$\Sigma_{\mathbf{Y}} = \mathbf{K} \Sigma_{\mathbf{X}} \mathbf{K}^T + \Sigma_{\mathbf{E}} \quad (26)$$

The source covariance matrix $\Sigma_{\mathbf{X}} = \sum_{i=1}^M \gamma_i \mathbf{X}_i$. γ_i and \mathbf{X}_i are the hyperparameter and covariance matrices of the i^{th} source. \mathbf{X}_i is the source covariance matrix defined prior. \mathbf{X}_i is zero except at the i^{th} element. This

term $\Sigma_{\mathbf{X}}$ imposes sparsity while minimizing the negative log marginal likelihood: The non-negative hyperparameter γ_i controls the row sparsity of \mathbf{X} . If $\gamma_i = 0$, the corresponding i^{th} source becomes zero. \mathbf{B} is a positive definite matrix capturing the correlation structure of \mathbf{X} . The sparsity is induced via the log term of the measurement covariance matrix in the likelihood. Finally, an optimization procedure that updates the hyperparameters γ_i in every iteration is performed. This is done by the evidence maximization update rule or fixed point gradient rule.

If sparsity is imposed on a source, it remains to be sparse. The SBL is known to converge fast. SBL solver assumes that the noise and covariances are more or less independent of time (Gramfort [2009]). In the real case scenario, the changes in γ_i occur over time. When the experiment is performed multiple times (trials) and when they are averaged leading to an evoked response, the source covariance matrix is very likely to change from the beginning to the latter (Gramfort [2009]). These are some issues for bSBL solvers.

3.5 Tensor based methods

Overview of Tensors: The generalization of 2D matrices is often called a tensor of order N . The size will be $n_1 \times n_2 \times \dots \times n_N$. The tensors can be factorized into a sum of a few component rank one tensors (Kolda and Bader [2009]). A third order tensor Γ of size $M \times N \times O$ can be decomposed as:

$$\Gamma = \sum_{k=1}^R \mathbf{I}_k \circ \mathbf{J}_k \circ \mathbf{K}_k \quad (27)$$

\circ represents the vector outer product. $\mathbf{I}_k, \mathbf{J}_k$, and \mathbf{K}_k are k^{th} rank one tensors of sizes $M \times 1, N \times 1$, and $O \times 1$ respectively. R is the rank of the tensor. The process of factorization is known as CP decomposition (canonical polyadic) (Kolda and Bader [2009]). The CP decomposition cannot be applied for tensors of order $N < 3$ or matrices. CPD is similar to singular value decomposition for matrices or specifically, CPD is the generalization of SVD.

The idea of tensor approaches for EEG source localization is to convert space-time EEG data into space-time-frequency domains which can be done employing a wavelet function. (Becker et al. [2014]) (Becker et al. [2012]).

$$\Gamma(\mathbf{r}, \tau, f) = \int_{-\infty}^{\infty} y_i(\mathbf{r}, t) \chi(s, t, \tau) dt \quad (28)$$

$y_i(\mathbf{r}, t)$ is the i^{th} channel EEG data. $\chi(s, t, \tau)$ is the wavelet function with scale s and center frequency f_c . The resulting \mathbf{F} is a function of space \mathbf{r} , time τ and frequency f . The frequency f can be estimated by $f = \frac{f_c}{sT}$. T is the interval between time samples and f_c is the center frequency. Instead of wavelet, local spatial Fourier transform can also be used (Becker et al. [2014]) (Becker et al. [2014]).

3.6 Extended source methods

The nature of source activations is locally clustered and globally sparse. The ℓ_2 norm and sparsity-based localization methods are good at predicting the active source locations. In clinical case studies like epilepsy, some issues arise. They are: (i) they fail to localize sources with a larger spatial extent, and (ii) they fail to discriminate close active sources (Becker et al. [2017]).

The spatial extent of the active source region becomes vital in detecting a focal epileptic zone. The epileptic activity spreads from one brain region to another. This leads to many highly correlated source regions being active simultaneously. To tackle such challenges, the well-known "cortical patch model" is introduced by (Limpiti et al. [2006]). A 'patch' is a set of pre-defined source regions. The beamforming approaches are utilized to identify sources that aim to describe the measurement vector.

Beamforming methods assume that the measurement data is generated by some cortical sources modeled by an equivalent set of current dipoles. The main issue with beamforming methods is the lack of the number of true sources that are responsible to explain the measurement vector. There are certain strategies to infer the number of true sources before solving the problem. A way of estimating the number is from the eigenvalue decomposition of the measurement covariance matrix. The eigenvalues drop and stay more or less flat. The number of indices n whose eigenvalues are of considerable magnitudes is treated as the number of active sources. In reality, it is quite difficult to see and perceive any kind of drop.

The 2q-th order Extended Source Multiple Signal Classification (2q-ExSo-MUSIC) algorithm (Biro et al. [2011]) and Disk Algorithm (DA) (Becker et al. [2014]) work on the principle of extended source localization. The 'extended source localization methods' aim to localize 'extended sources (or patches)' and works by using a beamforming strategy.

A cortical patch is modeled by many adjacent grid dipoles. Let p^{th} extended source Ω_p has the grid dipoles from $p = 1 \dots P$. The source space Ω_s is divided into extended source Ω_p and the rest of the sources. The rest

of the sources are assumed responsible to emit background activity in the brain.

$$\mathbf{X} = \sum_{\Omega_p} \mathbf{k}_p \mathbf{x}_p^T + \sum_{\Omega_b} \mathbf{k}_b \mathbf{x}_b^T = \mathbf{X}_p + \mathbf{X}_b \quad (29)$$

The \mathbf{X}_p explains the EEG data and \mathbf{X}_b indicates the background activity. The objective is to estimate the source signal matrix. The background activity is considered limited than the active source regions. The dipoles are estimated in the source patch Ω_p by thresholding the amplitudes of the estimated source signal. Some extended source strategies are reviewed below.

3.6.1 Variation-Based Sparse Cortical Current Distribution (VB-SCCD)

The idea of Variation-Based Sparse Cortical Current Distribution (VB-SCCD) (Ding [2009]) is to first transform the source domain to another domain that can track variations in current densities better. This is achieved using a linear transform \mathbf{V} to the source space. The source space is triangulated first such that each edge is only shared by two triangles. The operator is defined mathematically as:

$$\mathbf{V} = \begin{bmatrix} v_{11} & v_{22} & \dots & v_{1N} \\ \vdots & & \ddots & \vdots \\ v_{p1} & v_{2p} & \dots & v_{NP} \end{bmatrix}, \quad \begin{matrix} v_{ij} = 1; v_{ik} = -1; & i^{\text{th}} \text{ edge with } j, k \\ v_{ij} = 0 & \text{otherwise} \end{matrix} \quad (30)$$

\mathbf{V} is of size $P \times N$. P is the total number of edges of triangular elements. They will be non-zero values either 1 or -1. The cost function is:

$$\min \|\mathbf{V}\mathbf{X}\|_1 \text{ subject to } \|\mathbf{Y} - \mathbf{K}\mathbf{X}\|_2 \leq \epsilon \quad (31)$$

The variational map of sources $\|\mathbf{V}\mathbf{X}\|_1$ reveals the differences in amplitude between neighboring dipoles.

3.6.2 Source Imaging based on Structured Sparsity (SISSY)

The Variation-Based Sparse Cortical Current Distribution (VB-SCCD) (Ding [2009]) overcomes the challenge of localizing highly correlated sources. Moreover, the identification of close sources as separate sources remains a challenge. The close sources are identified as a single large one. The issue of neighboring sources is

tackled by Source Imaging based on Structured Sparsity (SISSY) (Becker et al. [2017]). The cost function of SISSY is:

$$\min_{\mathbf{X}} \frac{1}{2} \|\mathbf{Y} - \mathbf{KX}\|_F^2 + \lambda(\|\mathbf{VX}\|_1 + \alpha\|\mathbf{X}\|_1) \quad (32)$$

(i). SISSY incorporates an additional ℓ_1 norm to Eq. 31 to impose sparsity on estimated sources (Gramfort et al. [2013]). (ii). SISSY integrates ℓ_{21} norm to deal with the temporal structure of sources (Ou et al. [2009]). (iii) SISSY thresholds the background source activity using the 'Automatic thresholding' (AT). The source space is viewed as a graph with each source as a node. The edges between the sources are the edges of the graph. It is based on the watershed algorithm by (Vincent and Soille [1991]). The procedure of AT is as follows:

1. Applying watershed transforms on the edges of the graph.
2. The identified source regions are merged until only source regions that correspond to a local amplitude maximum or minimum remain.
3. The source regions that are responsible for EEG are identified by thresholding (10 % of maximum value)

3.6.3 Truncated Recursively Applied version- Multiple Signal Classification (TRAP-MUSIC)

Multiple Signal Classification (MUSIC) (Moshier and Leahy [1999]) is a well-known strategy. It (i) divides the measurement data into signal and noise subspaces and (ii) checks for each candidate source in the ROI whether it could explain the signal subspace or not (Liu and Schimpf [2006] Schmidt [1986]). RAP-MUSIC (Liu and Schimpf [2006] Moshier and Leahy [1999]) is a more sophisticated algorithm that can deal with the issues raised by classical MUSIC..

The TRAP-MUSIC (Mäkelä et al. [2018]) methodology is very similar to RAP - MUSIC. The only change is to the reduced signal subspace. The signal subspace is applied a dimensionality reduction at each recursion. The protocol behind the dimensionality reduction is as follows. As it is well known, at each recursion, one source is estimated and is projected out. For the next step, the same source need not be considered in the signal subspace. Let n be the true number of sources, \tilde{n} be the number of sources that are to be estimated. i be the recursion step. After, i^{th} step, the dimension of the remaining subspace is reduced to $\tilde{n} - i$.

In classical MUSIC, the local peaks of the localizer have to be estimated in one round. The number of peaks

gives the number of active dipoles and their source locations. Let $\mu(\mathbf{r})$ be the localizer which is a function of the source location \mathbf{r} .

$$\mu(\mathbf{r}) = \frac{\|\mathbf{R}_s \mathbf{k}(\mathbf{r})\|}{\|\mathbf{k}(\mathbf{r})\|} \quad (33)$$

\mathbf{R}_s is the signal space projection. In RAP-MUSIC, one global peak of the localizer has to be found out at every iteration. The localizer function will be at an iteration i is

$$\mu_i(\mathbf{r}) = \frac{\|\mathbf{R}_{s,i} \mathbf{Q}_i \mathbf{k}(\mathbf{r})\|}{\|\mathbf{Q}_i \mathbf{k}(\mathbf{r})\|} \quad (34)$$

\mathbf{Q}_i is the out projector. TRAP-MUSIC follows very similar procedure as of RAP- MUSIC except the estimation of transformed signal \mathbf{Q}_i . The procedure is as follows:

$$\begin{aligned} \mathbf{B}_i &= [\mathbf{k}_1 \dots \mathbf{k}_{i-1}] \\ \mathbf{Q}_i &= \mathbf{I} - \mathbf{B}_i \mathbf{B}_i^T \\ svd(\mathbf{Q}_i \mathbf{U}_s) &= \mathbf{U}_i \mathbf{\Lambda}_i \mathbf{V}_i^T \\ \mathbf{R}_i &= \mathbf{U}_i(:, 1 : \tilde{n}) \mathbf{U}_i^T(:, 1 : \tilde{n}) \\ \mu_i(\mathbf{r}_i) &= \frac{\|\mathbf{R}_{s,i} \mathbf{Q}_i \mathbf{k}(\mathbf{r})\|}{\|\mathbf{Q}_i \mathbf{k}(\mathbf{r})\|} \end{aligned} \quad (35)$$

\mathbf{B}_i has the topographies of previously estimated dipoles. \mathbf{k}_i is the local lead field matrix. Let $\mathbf{C} = \mathbf{Y}\mathbf{Y}^T$ be the covariance matrix of the measurement vector \mathbf{Y} . The \mathbf{C} has to be subdivided into signal subspace (\mathbf{C}_o) and noise subspace (\mathbf{C}_n). Let the measurement vector got added by white noise then, $\mathbf{C}_n = \sigma \mathbf{I}$. The covariance of the noiseless data is $\mathbf{C}_o = \mathbf{U}\mathbf{D}\mathbf{U}^T$, where \mathbf{U} is an $M \times M$ orthogonal matrix. $\mathbf{U}_s = [\mathbf{U}_1 \dots \mathbf{U}_n]$. n is the number of true sources. The eigenvalues $d_j, j = 1 \dots M$ will drop flat after d_n where n is the number of true sources. The need to compute $svd(\mathbf{Q}_i \mathbf{U}_s)$ is to find the orthogonal projection \mathbf{R}_i on to $span(\mathbf{Q}_i \mathbf{U}_s)$. i is the iteration step, $i = 1 \dots n$. the iteration is continued till a significant drop in the $\mu_i(\mathbf{r}_i)$ is observed. After $i > n$ a similar 'plateau' is observed.

3.7 Certainty based reduced sparse solution(CARSS)

There is no precise mathematical motivation behind discovering the method. However, it can be well studied through observations or intuitions and is justified by experiments (Mannepalli and Routray [2019]).

The certainty based reduced sparse solution - CARSS (Mannepalli and Routray [2019]) reduces the

solution space of an inverse problem to only the most certain active sources. This reduces the redundancy of the problem. Let a dipole in a voxel is active. The two key observations from the scalp potential of the dipole on which the method is developed are:

1. The 'peak' of the dipole and the 'shape' around the peak, is prominently evident in the measurement vector.
2. The region of evidence of the peak in the measurement vector is as it is for the dipole.

The prominent global extremum of the dipole on the scalp is referred to as the 'peak' of the dipole. Due to the sparse nature of activation, every peak of the active dipoles will be prominently evident in \mathbf{Y} .

The method utilizes the information provided by peaks in \mathbf{Y} to find the most certain sources that have generated the peaks observed in \mathbf{Y} . This method has a preliminary stage that has to be done only at the beginning. Stage-I reduces the solution space to the most certain sources. Stage-II solves the inverse problem with reduced solution space.

4 Challenges

The methods utilize advanced and robust mathematical tools. They are challenged by some difficulties and setbacks. The solution to the problem is challenged by some key factors. They are:

1. *Ill-posedness in the problem*: The problem in the real scenario is greatly ill-posed, making the methods tough to provide an accurate solution. Most of the methods could fail with an increase in the number of sources.
2. *Uncertainties/noise in the data*: The Bayesian methods and the ℓ_1 norm-based methods are known to provide accurate solutions to many problems. However, they are also sensitive to noise. The ITER's too are known to mislead the solution under noise.

The instantaneous solvers solve the problem instant by instant independent of each other. This leads to an implication that the signal, and hence the noise is independent of time. This is reported to be a challenging assumption as the nature of the 'signal' may change with time but 'noise' may not during an evoked response (Gramfort et al. [2012]). The noise is usually estimated when the brain is not yet under any stimulus. Besides, there will be measurement noise due to the electrode channels. These all factors may be the issues for instantaneous solvers dealing with noisy data although they prove to be successful.

3. *Sparsity in the solution*: The source activation is not sparse at any time. The sources show an oscillatory activity but not spiky activity. However, the solution is considered to be sparse during an evoked response study. The averaging over trials (repeated experiments) results in suppression of sources, not of interest. The sparsity promoting $\ell_{p,p} < 1$ norm is known to provide a sparse solution. The $\ell_{p,p} \leq 1$ is non-convex. The ℓ_1 norm is convex and can provide sparse solutions. The ℓ_2 norm provides the root of a squared sum due to which it cannot provide a sparse solution. The characteristic of the ℓ_2 norm does not allow sparsity. The $\ell_{p,p} < 1$ solvers produce sparse solutions while ℓ_2 based solvers cannot. The ℓ_{21} norm is at an advantage since it allows link-up between ℓ_2 and ℓ_1 norms.
4. *Comprehensible Results*: The ℓ_2 norm is known to provide a smooth gradient in its solution. The ℓ_1 norm can handle noise well than the ℓ_2 norm. The typical MAP estimators with Gaussian likelihood and ℓ_1 norm regularization estimators lead to convex optimization problems and will lead to a unique solution. The FOCUSS is known to provide a scattered solution under noise. FOCUSS works to minimize a non-convex ℓ_0 norm cost function.
5. *Computational time*: In general, many methods provide accuracy by sacrificing computational time. Some methods are too slow to converge. The computation of the inverse of a large matrix, in general, is computationally expensive.
6. *Convergence issues*: some methods converge to the local minima instead of global. An example is FOCUSS. Some have convergence issues under noise.
7. *Complying with the ground reality*: Although mathematically well understood and modeled, the solution should be aligned with various anatomical and physiological constraints and realities.

5 Comparative Study

The toolbox utilized for the current study is SEREEGA: Simulating Event-Related EEG Activity developed by (Krol et al. [2018]). All the computations are performed in an x64-bit, 8 GB RAM, Intel(R) core processor Laptop.

The head model employed is the 'New-York Head model (ICBM-NY)' (Huang et al. [2016]). The lead-field matrices are of size $64 \times 15,012$ and $64 \times 6,004$. The number of sources is 5,001 and 2,001. The whole computations of generating the EEG signals are performed in the SEREEGA toolbox (Krol et al. [2018]). The length of the measurement matrix \mathbf{Y} simulated is of 1000 sample size.

Sparse Bayesian Learning based methods are implemented according to (Zhang and Rao [2011]) and (Wipf et al. [2011]). For, SBL according to (Wipf et al. [2011]), the sparsity data-fit balancing parameter λ is considered 0.2. For, (Zhang and Rao [2011]), the threshold for pruning small hyperparameters is set to 10^{-3} . The maximum iterations performed are 50. Mixed norm estimate is implemented according to (Gramfort et al. [2012]). sLORETA is implemented according to (Pascual-Marqui et al. [2002]). The regularization parameter is calculated using 'l-curve' method (Hansen and O'Leary [1993]) wherever needed.

A' metric: A' metric estimates the area under the ROC for one HR/FR pair. The Hit rate (HR) is defined as the number of hits. A 'hit' means that the source is localized correctly. False-positive rate (FR) indicates the number of false positives. The higher A' metric value indicates a high hit rate compared to the false positive rate. A' metric estimates the area under the ROC curve.

$$A' = \frac{(HR - FR) + 1}{2} \quad (36)$$

ROC in general means receiver-operator characteristic (Oikonomou and Kompatsiaris [2020] Snodgrass and Vanderwart [1980] Darvas et al. [2004]). To estimate the local peak, the procedure as presented in (Wipf et al. [2010]) is followed.

Success rate (SR): A 'hit' for a true source is defined when there is at least one local peak formed within a certain neighborhood of the source's location. (Wipf et al. [2010]). The region under consideration is a sphere centered at the true source location and two levels of neighboring sources. SR can be 1 or 0 for a true source. In the aforementioned test cases, the success rate for each source is estimated and the results are tabulated.

5.1 Monte-carlo simulations

Four test cases are considered. The random sources with orientation are chosen using in SAREEGA toolbox (Krol et al. [2018]). The performance metric is A metric (Wipf et al. [2010]). Each test case has three noise levels - no noise added, pink noise of amplitude one (Krol et al. [2018]) (Haufe and Ewald [2019]) and of amplitude four. The number of possibilities considered for each test case will be 360. The detailed breakup is shown below.

1. The total number of test-cases is 4.
 Test Case-I: one source.

Test Case-II: three sources.

Test Case-III: five sources.

Test Case-IV: seven sources.

2. Each test-case has three noise levels added.
 No noise added.
 pink noise of amplitude one is added.
 pink noise of amplitude four is added.
3. Each noise level is evaluated for two source spaces.
 Five-K source space (has $5,001 \times 3 = 15,001$ sources).
 Two-K source space (has $2,001 \times 3 = 6,001$ sources).
4. Each source space is further estimated with and without CARSS.
 Not reduced by CARSS.
 The reduced solution space by CARSS.
5. The total number of samples considered is 30.

The ERP is as shown in Fig. 4. The peak latencies of the ERP are 500, 300, and 200 ms. The peak widths are 200, 300, and 100 ms. The peak amplitudes are 1, 1.2, and $0.6 \mu V$.

TEST-CASE I: Thirty sources with random orientations are chosen. No constraint on the position or orientation of the source is applied. The source can be a deep or shallow one. The results are shown in Table. 1. The source information is given in Fig. 2. The results are depicted in Tables 1, 2 and 3.

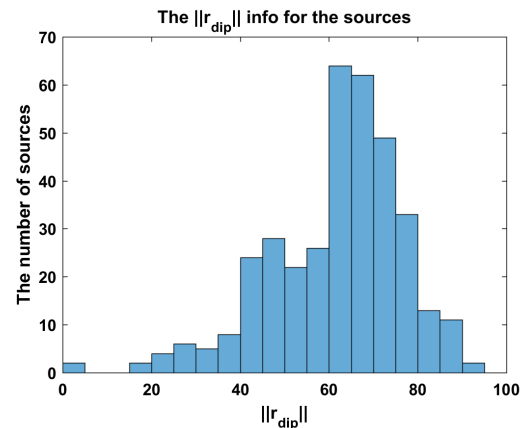


Fig. 2 TEST CASE-I: The r_{dip} (in mm) of all the possibilities (360 in total).

TEST-CASE II: Three sources with random orientation has been chosen. They are chosen such that (i) $Ds(\mathbf{r}_i, \mathbf{r}_j) \geq 80, i, j = 1 \dots 30$, and (ii) $r_i \geq 90, i = 1 \dots 30$. The information about the sources chosen is given in Table. 4. The total number of possibilities is 360. The results are depicted in Tables 5, 6 and 7.

S.No.	Method	without CARSS			with CARSS		
		Non	p - 1	p - 4	Non	p - 1	p - 4
1	FOCUSS	0.92	0.60	0.44	0.99	0.78	0.55
2	MxNE	0.62	0.58	0.46	0.86	0.82	0.76
3.	SBL WIPF	0.60	0.56	0.47	0.90	0.78	0.65
4	SBL- Zhang	0.61	0.57	0.47	0.85	0.79	0.76
5	sLORETA	0.60	0.56	0.41	0.82	0.75	0.55

S.No.	Method	without CARSS			with CARSS		
		Non	p - 1	p - 4	Non	p - 1	p - 4
1	FOCUSS	0.90	0.69	0.50	0.98	0.88	0.71
2	MxNE	0.87	0.76	0.65	0.97	0.95	0.89
3.	SBL WIPF	0.85	0.69	0.55	0.98	0.90	0.78
4	SBL- Zhang	0.84	0.70	0.62	0.98	0.94	0.90
5	sLORETA	0.75	0.65	0.55	0.90	0.85	0.77

Table 1 TEST-CASE I: The A' metric values observed for 5K (left) - and 2K (right) source space.

S.No.	Method	without CARSS			with CARSS		
		Nonon	p - 1	p - 4	Nonon	p - 1	p - 4
1.	FOCUSS	+4 to -6	+8 to -7.5	+9 to -11	+2 to -3	+3.5 to -6	+7.3 to -2.6
2.	MxNE	+3 to -5	+4.8 to -5	+6.6 to -7	+1.8 to -2.5	+2.5 to -4.1	+3.35 to -2.73
3.	SBL - Wipf	+2 to -6	+3.6 to -4.52	+5.9 to -8.5	+1.7 to -1.6	+3.2 to -1.2	+4.2 to -5.7
4.	SBL - Zhang	+2.5 to -3.5	+3.3 to -3.9	+4.6 to -5.85	+1.8 to -2.0	+3.3 to -2.95	+4.8 to -4.2
5.	sLORETA	+4.5 to -3.6	+5.2 to -3.2	+6.6 to -4.5	+2.9 to -3.5	+4.4 to -4.2	+5.7 to -5.1

S.No.	Method	without CARSS			with CARSS		
		Nonon	p - 1	p - 4	Nonon	p - 1	p - 4
1.	FOCUSS	+3.6 to -4	+7.5 to -8	+9.5 to -8.9	+2.05 to -2.3	+3 to -5.65	+8.9 to -7.7
2.	MxNE	+2.5 to -3.4	+4.05 to -3.65	+6.85 to -6.55	+1.1 to -1.75	+1.3 to -2.6	+2.85 to -2.25
3.	SBL - Wipf	+2.25 to -3.75	+3.20 to -4.20	+5.5 to -6.65	+1.8 to -1.45	+2.85 to -1.60	+3.95 to -4.25
4.	SBL - Zhang	+2.85 to -3.15	+3.95 to -3.50	+4.90 to -4.65	+1.15 to -2.0	+2.8 to -2.05	+4.25 to -4.85
5.	sLORETA	+3.5 to -3.9	+6.2 to -1.85	+6.15 to -5.5	+2.15 to -2.35	+3.65 to -3.05	+4.55 to -4.35

Table 2 TEST-CASE I: The 95% Conf. Int. [upper limit, lower limit] of the A' metric values observed for 5K (up) - and 2K (down) source space.

S.No.	Noise level	Five - K (15,000)			Two - K (6, 000)		
		Avg.	Mar.	Min.	Avg.	Mar.	Min.
1.	No noise	2531	3725	732	1367	1852	990
2.	pink - 1	2916	3678	870	1351	1670	576
3.	pink - 4	3373	4415	2191	1335	1852	413

Table 3 TEST CASE- I: The no. of sources CARSS reduced to is presented

Sources	$\ r\ _{dip}$	S-I	S-II	S-III
S-I	94.8	-	110.5	100.9
S-II	116.7	110.0	-	120.5
S-III	81.2	100.9	110.5	-

Table 4 The distance between each source $Ds(\mathbf{r}_i, \mathbf{r}_j)$ and their radius of curvature $\|r\|_{dip}$

TEST-CASE - III: Five sources are chosen . Their conditions for selection are: (i) Three deep sources $\mathbf{r}_{dip} \leq 60$ (ii) An intermittent source $80 \leq \mathbf{r}_{dip} \leq 60$ (iii) Distance between the sources $Ds(\mathbf{r}_i, \mathbf{r}_j) \geq 70$, and a (iv) shallow source $\mathbf{r}_{dip} \geq 70$. The information about the sources chosen is given in 8. The results are depicted in Tables 9, 10 and 11.

TEST-CASE IV: Seven sources are chosen . Their conditions for selection are: (i) Four deep sources distance between them is $Ds(\mathbf{r}_i, \mathbf{r}_j) \leq 55$ (ii) An intermittent source $60 \leq \mathbf{r}_{dip} \leq 70$, and (iii) two shallow source $\mathbf{r}_{dip} \geq 70$. The information about the sources is given in Table. 12. The results are depicted in Tables 13, 14 and 15.

5.2 CARSS evaluation

The detailed analysis of CARSS is evaluated in (Mannepalli and Routray [2019]). However, two challenging possibilities arise for any source localization method in general. They are (i) deep sources and (ii) near sources.

In this work, the aforementioned aspects of CARSS are analyzed.

DEEP SOURCES: Estimation of deep sources is a challenge for any source localization method. The evidence of the peak is critical for CARSS to detect. Thirty deep sources whose $\|r\|_{dip} \leq 40$ are chosen. The $\mu(\|r\|_{dip})$ is 27.5. CARSS detected all the deep sources even under the presence of noise comfortably. The only issue if at all arise is the number of certain sources. The results are presented in Table. 18. Only 5K-source space is considered.

DEEP SOURCE AND ITS NEAR SOURCE: A deep source whose $\|r\|_{dip} \leq 40$ and its near-source whose $Ds(r_{dip,i}, r_{dip,j}) \leq 40$ are chosen . The results are presented in Table. 19. Only 5K-source space is considered. The results show inconsistency. Although CARSS succeeded half of the possibilities, it could not guarantee all.

5.3 Extended source algorithms

Two test cases are considered. Thirty simulations are performed for each test case with randomly chosen sources. The random sources with orientation are chosen using in SAREEGA toolbox (Krol et al. [2018]). The methods aimed to be studied are Truncated RAPMUSIC (Mäkelä et al. [2018]) and Source Imaging based on Structured Sparsity (SISSY) (Becker et al. [2017]). The motivation behind the study is not to compare the methods but is how well the integration with CARSS will go. The initial estimate of the number of sources considered is $\tilde{n} = n + 2$.

The performance metric utilized is Dipole Localization Error (DL_e) (Yao and Dewald [2005]) and Spatial Dispersion (Zhu et al. [2014] Molins et al. [2008]). The DL_e investigates the similarity between true source configuration and the estimated. Let n and \tilde{n} be the number of true and estimated dipoles and let I and \tilde{I}

S.No.	Method	without CARSS			with CARSS		
		Non	p - 1	p - 4	Non	p - 1	p - 4
1	FOCUSS	0.55	0.10	0.05	0.82	0.26	0.10
2	MxNE	0.42	0.30	0.21	0.61	0.50	0.35
3.	SBL WIPF	0.39	0.20	0.06	0.66	0.45	0.12
4	SBL- Zhang	0.31	0.30	0.15	0.55	0.45	0.24
5	sLORETA	0.26	0.22	0.12	0.45	0.27	0.14

S.No.	Method	without CARSS			with CARSS		
		Non	p - 1	p - 4	Non	p - 1	p - 4
1	FOCUSS	0.65	0.22	0.10	0.82	0.29	0.20
2	MxNE	0.51	0.44	0.38	0.76	0.72	0.60
3.	SBL WIPF	0.50	0.29	0.16	0.80	0.33	0.21
4	SBL- Zhang	0.45	0.39	0.20	0.70	0.59	0.48
5	sLORETA	0.39	0.26	0.16	0.45	0.21	0.10

Table 5 TEST-CASE II: The A' metric values observed for 5K (left) - and 2K (right) source space.

S.No.	Method	without CARSS			with CARSS		
		Nonon	p - 1	p - 4	Nonon	p - 1	p - 4
1.	FOCUSS	4 to -3	+14 to -16	+25 to -19	+3 to -3	+ 7 to -11	+ 15 to -14
2.	MxNE	+3 to -4	+ 5 to -3	+ 7 to -5	+ 2 to -5	+6 to -4	+5 to -6
3.	SBL - Wipf	+4 to -6	+6 to -5	+7 to -5	+3 to -3	+4 to -2	+4 to -4
4.	SBL -Zhang	+4 to -6	+ 5 to -3	+6 to -7	+3 to -3	+5 to -4	+6 to -5
5.	sLORETA	+5 to -5	+6 to -5	+7 to -7	+4 to -3	+5 to -4	+7 to -3

S.No.	Method	without CARSS			with CARSS		
		Nonon	p - 1	p - 4	Nonon	p - 1	p - 4
1.	FOCUSS	5 to -2	+9 to -11	+25 to -19	+4 to -3	+ 8 to -10	+ 17 to -12
2.	MxNE	+3 to -3	+ 4 to -3	+ 6 to -5	+ 2 to -5	+3 to -3	+4 to -6
3.	SBL - Wipf	+3 to -4	+5 to -5	+8 to -6	+3 to -3	+6 to -4	+6 to -6
4.	SBL -Zhang	+3 to -4	+ 4 to -4	+5 to -4	+3 to -3	+4 to -4	+5 to -5
5.	sLORETA	+4 to -4	+5 to -4	+6 to -5	+3 to -3	+4 to -4	+7 to -5

Table 6 TEST-CASE II: The 95% Conf. Int. [upper limit, lower limit] of the A' metric values observed for 5K (left) - and 2K (right) source space. The % values are given in the table.

S.No.	Noise level	Five - K (15,000)			Two - K (6, 000)		
		Avg.	Max.	Min.	Avg.	Max.	Min.
1.	No noise	3646	4849	1503	1767	2372	958
2.	pink - 1	4248	5870	1735	1955	2925	1281
3.	pink - 4	4478	6280	2051	2255	1590	2925

Table 7 TEST CASE- II: The table shows the no. of sources CARSS reduced the solution space is presented

S.No.	$\ r_{dip}\ $	S-I	S-II	S-III	S-IV	S-V
S-I	39.7	-	72.2	100.8	81.2	110.0
S-II	44.8		-	69.8	92.6	102.5
S-III	62.6			-	96.6	76.2
S-IV	74.9				-	122.1
S-V	90.6					-

Table 8 The distance between each source $Ds(\mathbf{r}_i, \mathbf{r}_j)$ and their radius of curvature $\|r\|_{dip}$

be the true and estimated set of dipole indices of the active patch. The DLe is defined as:

$$DLE = \frac{1}{2n} \sum_{k \in I} \min_{V1} \|\mathbf{r}_k - \mathbf{r}_1\| - \frac{1}{2\tilde{n}} \sum_{l \in \tilde{I}} \min_{V_k} \|\mathbf{r}_1 - \mathbf{r}_k\| \quad (37)$$

The SD estimates the spatial blur of estimated sources as compared with the same of true sources.

$$SD = \sqrt{\frac{\sum_{p=1}^{N_s} \sum_{q=d_n} d_{pq}^2 \|\tilde{s}_q\|_2^2}{\sum_{q=1}^{N_s} \|\tilde{s}_q\|_2^2}} \quad (38)$$

Understanding the equations in simpler terms, they can be described as (i) DLe is the average distance of the maxima of the estimated source to the true sources, and (ii) SD is the spatial extent of the estimated source as compared to the same of the true source.

TEST-CASE (Ext.)-I:

One source with random orientation is considered. The performance of the methods with CARSS is better than without. CARSS reduced the source space giving fewer sources to search in. Both the methods located the dipoles correctly. The 95 % confidence limit over the mean is mentioned. The number of sources is estimated as one by the methods ($\tilde{n} = n + 2$;). In TRAP-MUSIC, a significant drop in the scanning value of the localizer (μ_i) shown a significant drop just as (Mäkelä et al. [2018]) after $n = 1$.

The results are presented in Table. 20 and Table. 21.

TEST-CASE (Ext.) II

Three deep sources with random orientations are considered. The performance of the methods with CARSS is better than without. CARSS reduced the source space giving fewer sources to search in. The 95 % confidence limit over the mean is mentioned. The results are presented in Table. 22 and Table. 23. the number of sources is estimated as three by the methods ($\tilde{n} = n + 2$;). In TRAP-MUSIC, a significant drop in the scanning value of the localizer ($\mu_i, i = 1 \dots \tilde{n}$) shown a significant drop just as (Mäkelä et al. [2018]) after $n = 3$.

5.4 Real data experiment

The data utilized for the current study is downloaded from <http://kdd.ics.uci.edu/databases/eeg/eeg.html>. The aim of the study to examine EEG correlates of genetic predisposition to alcoholism (Ingber [1997]) (Ingber [1998]) (Snodgrass and Vanderwart [1980]). It contains measurements from 64 electrodes placed on the scalp sampled at 256 Hz (3.9-msec epoch) for 1 second.

There were two sets of subjects: the alcoholic group and the control group. Each subject was exposed to

S.No.	Method	without CARSS			with CARSS		
		Non	p - 1	p - 4	Non	p - 1	p - 4
1	FOCUSS	0.20	0.01	0.01	0.32	0.05	0.01
2	MxNE	0.14	0.10	0.05	0.22	0.14	0.09
3.	SBL WIPF	0.10	0.02	0.01	0.25	0.09	0.05
4	SBL- Zhang	0.19	0.11	0.05	0.18	0.13	0.10
5	sLORETA	0.15	0.08	0.04	0.17	0.10	0.08

Table 9 TEST-CASE III: The A' metric values observed for 5K (left) - and 2K (right) source space.

S.No.	Method	without CARSS			with CARSS		
		Nonon	p - 1	p - 4	Nonon	p - 1	p - 4
1.	FOCUSS	7 to -5	+22 to -20	+35 to -49	+6 to -3	+ 17 to -14	+ 30 to -15
2.	MxNE	+5 to -4	+ 8 to -7	+ 9 to -9	+ 4 to -6	+6 to -7	+6 to -8
3.	SBL - Wipf	+7 to -4	+9 to -7	+ 10 to - 9	+4 to -5	+6 to -7	+8 to -8
4.	SBL -Zhang	+7 to -5	+ 8 to -6	+7 to -8	+6 to -5	+6 to -6	+7 to -6
5.	sLORETA	+9 to -5	+8 to -8	+7 to -10	+4 to -4	+6 to -7	+7 to -7

Table 10 TEST-CASE III: The 95% Conf. Int. [upper limit, lower limit] of the A' metric values observed for 5K (left) - and 2K (right) source space. The % values are given in the table.

S.No.	Noise level	Five - K (15,000)			Two - K (6, 000)		
		Avg.	Max.	Min.	Avg.	Max.	Min.
1.	No noise	4745	6961	2598	2231	2781	1713
2.	pink - 1	5284	7656	2691	2381	3508	1685
3.	pink - 4	5417	7331	3379	2603	3601	1145

Table 11 TEST CASE- III: The no. of sources CARSS reduced to is presented

S.No.	S-I	S-II	S-III	S-IV	S-V	S-VI	S-VII
S-I		49.2	50.8	53.8	69.7	76.9	75.9
$\ r_{dip}\ $	36.2	46.7	59.5	66.4	83.7	92.8	96.8

Table 12 The distance between S-I and each source $Ds(\mathbf{r}_i, \mathbf{r}_j)$ and their radius of curvature $\|r\|_{dip}$

either a single stimulus (S1) or to two stimuli (S1 and S2) which were pictures of objects chosen from the 1980 Snodgrass and Vanderwart picture set. When two stimuli were shown, they were presented in either a matched condition where S1 was identical to S2 or in a non-matched condition where S1 differed from S2.

The three versions of the EEG data set are provided. The small dataset version has two subjects - one from alcoholics and the other from the control group. For each subject, three matching paradigms are provided. They are c_1 (one presentation only), c_m (match to the previous presentation) and c_n (no-match to the previous presentation). Ten trial runs are given. For the current study, a small dataset is utilized. The large dataset has 120 trials for 120 subjects. The objective of the current study does not fit considering large data hence the small dataset is chosen.

5.5 Simulated data tests

Test Case-I:

S.No.	Method	without CARSS			with CARSS		
		Non	p - 1	p - 4	Non	p - 1	p - 4
1	FOCUSS	0.37	0.01	0.01	0.39	0.05	0.01
2	MxNE	0.26	0.22	0.16	0.33	0.26	0.17
3.	SBL WIPF	0.22	0.12	0.01	0.26	0.15	0.02
4	SBL- Zhang	0.23	0.18	0.15	0.37	0.30	0.21
5	sLORETA	0.17	0.11	0.06	0.21	0.16	0.11

S.No.	Method	without CARSS			with CARSS		
		Nonon	p - 1	p - 4	Nonon	p - 1	p - 4
1.	FOCUSS	6 to 5	+20 to -16	+30 to -36	+5 to -5	+ 16 to -11	+ 25 to -16
2.	MxNE	+4 to -3	+ 7 to -5	+ 6 to -7	+ 4 to -2	+6 to -8	+5 to -9
3.	SBL - Wipf	+6 to -3	+9 to -6	+ 10 to - 10	+3 to -4	+6 to -5	+8 to -9
4.	SBL -Zhang	+6 to -4	+ 8 to -5	+8 to -8	+6 to -6	+5 to -6	+8 to -6
5.	sLORETA	+7 to -7	+8 to -8	+10 to -10	+5 to -5	+6 to -7	+7 to -7

The dipole is located at [17.08, -4.21, 75.74] mm oriented along [1,0,0] is activated. The distance from the origin of Source-I $\|\mathbf{r}\|$ (S-I) is 77 mm.

The ERP is as shown in Fig. 4. The peak latencies of the ERP are 500, 300, and 200 ms. The peak widths are 200, 300, and 100 ms. The peak amplitudes are 1, 1.2, and 0.6 μ V.

The sensor noise of amplitude 5% and 10% are added to the noiseless measurement data. This noise has no dependencies across channels or samples.

The CARSS identified all the sources and reduced the SS to 875 out of 15012 in the 5K-SS. The CARSS identified all the sources and reduced the SS to 1256 out of 6012 in the 2K-SS. The sources are identified even under the presence of noise.

The details can be observed from Fig. 4.

Test Case-II:

The dipoles are located at [-39.2764, 42.20, 35.88] mm, [28.77, -74.93, 53.13] mm, and [55.69, -7.10, -41.42] mm oriented along [1,0,0], [0,1,0], and [0,0,1] are activated. All the three ERPs are the same as shown in Fig. 5. The peak latencies of the ERP are 500, 400, and 300 ms. The peak widths are 200, 100 and 200 ms. The peak amplitudes are 1, 1.2, and 0.8 μ V.

1. Distance from the origin $\|\mathbf{r}_i\|, i = 1$ of S-I is 67.9 mm. Distance between S-I and others $\|\mathbf{r}_{i,j}\|, j = 2 \dots 5$ is 136.6 mm.
2. Distance from the origin $\|\mathbf{r}_i\|, i = 2$ of S-II is 96.3 mm. Distance between S-II and others $\|\mathbf{r}_{i,j}\|, j = 2, 3$ is 119.4 mm.
3. Distance from the origin $\|\mathbf{r}_i\|, i = 3$ of S-III is 69.8 mm.

The brown noise of amplitude one and four are added to the noiseless measurement data. There is no such specific aim in adding brown noise.

S.No.	Method	without CARSS			with CARSS		
		Non	p - 1	p - 4	Non	p - 1	p - 4
1	FOCUSS	0.0500	0.0001	0.0001	0.3200	0.0006	0.0001
2	MxNE	0.0900	0.0100	0.0040	0.1100	0.0400	0.0160
3	SBL WIPF	0.0700	0.0001	0.0001	0.1200	0.0002	0.0001
4	SBL- Zhang	0.0600	0.0080	0.0010	0.1000	0.0500	0.0080
5	sLORETA	0.0020	0.0005	0.0001	0.0800	0.0100	0.0005

S.No.	Method	without CARSS			with CARSS		
		Non	p - 1	p - 4	Non	p - 1	p - 4
1	FOCUSS	0.1000	0.0001	0.0001	0.3200	0.0008	0.0001
2	MxNE	0.1800	0.0600	0.0200	0.1900	0.0800	0.0250
3	SBL WIPF	0.1100	0.0001	0.0001	0.1300	0.0003	0.0001
4	SBL- Zhang	0.1000	0.0600	0.0300	0.1000	0.0900	0.0060
5	sLORETA	0.0020	0.0010	0.0001	0.0030	0.0100	0.0005

Table 13 TEST-CASE IV: The A' metric values observed for 5K (left) - and 2K (right) source space.

S.No.	Method	without CARSS			with CARSS		
		Nonon	p - 1	p - 4	Nonon	p - 1	p - 4
1.	FOCUSS	+8 to +10	+45 to -40	+46 to -46	+7 to -9	+40 to -40	+45 to -38
2.	MxNE	+8 to -9	+10 to -11	+10 to -14	+8 to -8	+10 to -12	+9 to -14
3.	SBL - Wipf	+8 to -6	+11 to -12	+14 to -15	+8 to -7	+10 to -11	+15 to -15
4.	SBL -Zhang	+8 to -8	+10 to -12	+10 to -15	+8 to -8	+10 to -10	+13 to -12
5.	sLORETA	+7 to -10	+12 to -12	+12 to -14	+7 to -11	+10 to -12	+10 to -14

S.No.	Method	without CARSS			with CARSS		
		Nonon	p - 1	p - 4	Nonon	p - 1	p - 4
1.	FOCUSS	+9 to -9	+45 to -35	+45 to -45	+7 to -7	+40 to -40	+45 to -45
2.	MxNE	+7 to -9	+9 to -10	+10 to -11	+7 to -7	+9 to -9	+10 to -11
3.	SBL - Wipf	+6 to -7	+10 to -10	+15 to -15	+8 to -8	+10 to -10	+14 to -14
4.	SBL -Zhang	+8 to -8	+9 to -9	+12 to -12	+7 to -7	+8 to -8	+11 to -11
5.	sLORETA	+10 to -10	+12 to -12	+16 to -16	+8 to -8	+10 to -10	+15 to -15

Table 14 TEST-CASE IV: The 95% Conf. Int. [upper limit, lower limit] of the A' metric values observed around mean for 5K (left) - and 2K (right) source space. The % values are given in the table.

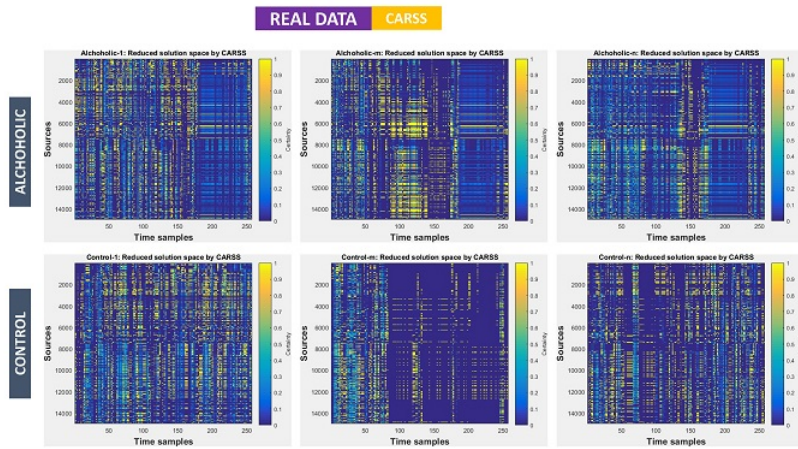


Fig. 3 REAL DATA: The reduced solution space by CARSS is presented. The x-axis represent time samples and y-axis represent sources indices. CARSS reduced between 8 % to 30 % of the total solution space.

S.No.	Noise level	Five - K (15,000)			Two - K (6,000)		
		Avg.	Max.	Min.	Avg.	Max.	Min.
1.	No noise	5929	2952	6327	1826	319	2260
2.	pink - 1	6117	2997	7571	2125	1080	2284
3.	pink - 4	.7963	3377	9813	4117	2952	5335

Table 15 TEST CASE- IV: The no. of sources CARSS reduced to is presented

The CARSS identified all the sources and reduced the SS to 4258 out of 15012 in the 5K-SS. The CARSS identified all the sources and reduced the SS to 1313 out of 6012 in the 2K-SS. The sources are identified even under the presence of noise.

The details can be observed from Fig. 5.

Test case-III

The dipoles are located at $[-35.65, 5.63, 38.84]$ mm, $[-65.19, -39.30, -14.21]$ mm, $[15.45, -27.58, 73.34]$ mm, $[39.05, -73.27, -3.30]$ mm, and $[-32.99, 60.39, 13.64]$ mm oriented along $[1,0,0]$, $[0,1,0]$, $[0,0,1]$, $[0,1,0]$ and $[1,0,0]$ are activated. All the three ERPs are the same as shown

in Fig. 6. The peak latencies are 500, 400, and 300 ms. The peak widths are 200, 100 and 200 ms. The peak amplitudes are 1, 1.2, and $0.8 \mu V$.

1. Distance from the origin $\|\mathbf{r}_i\|$, $i = 1$ of S-I is 53.0 mm. Distance between S-I and others $\|\mathbf{r}_{i,j}\|$, $j = 2 \dots 5$ is 113.1 mm.
2. Distance from the origin $\|\mathbf{r}_i\|$, $i = 2$ of S-II is 77.4 mm. Distance between S-II and others $\|\mathbf{r}_{i,j}\|$, $j = 3 \dots 5$ is 119.6 mm.
3. Distance from the origin $\|\mathbf{r}_i\|$, $i = 3$ of S-III is 79.9 mm. Distance between S-I and others $\|\mathbf{r}_{i,j}\|$, $j = 4, 5$ is 103.7 mm.
4. Distance from the origin $\|\mathbf{r}_i\|$, $i = 4$ of S-VI is 101.2 mm. Distance between S-IV and others $\|\mathbf{r}_{i,j}\|$, $j = 5$ is 170 mm.
5. Distance from the origin $\|\mathbf{r}_i\|$, $i = 5$ of S-V is 70.4 mm.

TEST CASE	TC-1		TC-2		TC-3						TC-4					
	<i>S-I</i> [30]	<i>S-I</i> [30]	<i>S-I,II,III</i> [90]	<i>S-I,II,III</i> [90]	<i>3 deep</i> [30]	<i>1 int.</i> [10]	<i>1 shall.</i> [10]	<i>3 deep</i> [30]	<i>1 int.</i> [10]	<i>1 shall.</i> [10]	<i>4 deep</i> [40]	<i>1 int</i> [10]	<i>2 shall.</i> [20]	<i>4 deep</i> [40]	<i>1 int</i> [10]	<i>2 shall.</i> [20]
	without CARSS	with CARSS	without CARSS	with CARSS	without CARSS			with CARSS			without CARSS			with CARSS		
FOCUSS	30,29,29	30,30,30	85,78,72	90,86,80	19,6,1	8,2,2	9,6,4	21,7,2	9,1,2	10,7,6	5,0,0	6,1,1	15,6,1	6,0,0	7,1,1	17,8,7
MxNE	30,30,30	30,30,30	84,85,78	90,90,89	20,16,12	7,6,5	9,8,8	22,18,16	10, 8,7	10,10,9	8,5,2	7,6,4	14,11,9	9,8,6	8,7,6	18, 15,14
SBL - Wipf	30,30,30	30,30,30	89,82,76	90,82,81	21,13,9	9,6,4	9,8,7	25,16,11	10,6,4	10,8,8	6,2,0	6,4,2	13,7,5	5,3,1	7,6,4	14,12,10
SBL - Zhang	30,30,30	30,30,30	88,82,78	90,88,86	19,15,12	8,7,6	9,9,7	23,19,16	10,9,8	10,10,9	7,6,6	7,7,5	14,11,8	9,7,7	8,6,6	16,15,13
sLORETA	30,29,29	30,30,30	85,80,76	90,86,78	15,11,8	7,6,5	8,7,6	18,14,10	8,7,6	10,9,8	5,4,2	6,4,4	11,9,8	5,5,5	8,5,5	12,10,8

Table 16 The success rate (SR) for the sources in all the test cases in the 5K-SS. The three values in each cell designate the case when no-noise, pink noise of amplitude one and four are considered. 'deep' indicates deep sources, 'int.' indicates intermittent sources and 'shall.' indicates shallow sources

TEST CASE	TC-1		TC-2		TC-3						TC-4					
	<i>S-I</i> [30]	<i>S-I</i> [30]	<i>S-I,II,III</i> [90]	<i>S-I,II,III</i> [90]	<i>3 deep</i> [30]	<i>1 int.</i> [10]	<i>1 shall.</i> [10]	<i>3 deep</i> [30]	<i>1 int.</i> [10]	<i>1 shall.</i> [10]	<i>4 deep</i> [40]	<i>1 int</i> [10]	<i>2 shall.</i> [20]	<i>4 deep</i> [40]	<i>1 int</i> [10]	<i>2 shall.</i> [20]
	without CARSS	with CARSS	without CARSS	with CARSS	without CARSS			with CARSS			without CARSS			with CARSS		
FOCUSS	30,30,29	30,30,30	90,88,82	90,89,88	20,6,5	9,6,5	10,5,2	21,10, 6	10,7,5	10,8,6	8,2,1	7,2,3	16,5,2	8,3,3	7,4,3	16,9,2
MxNE	30,30,30	30,30,30	90,86,82	90,90,90	22,18,16	8,7,6	10,8,8	25,19,18	10, 8,7	10,10,9	9,8,7	8,6,5	15,12,10	10,8,8	8,8,6	19,17,15
SBL - Wipf	30,30,30	30,30,30	90,88,86	90,89,88	23,15,10	10,6,4	10,7,7	25,17,12	10,7,5	10,8,8	9,7,2	8,5,4	17,10,5	9,8,2	8,6,3	16,11,9
SBL - Zhang	30,30,30	30,30,30	90,90,88	90,90,90	22,18,15	10,8,6	10,9,7	25,20,18	10,9,8	10,10,9	8,6,5	8,7,6	16,11,11	9,6,5	8,7,7	16,12,13
sLORETA	30,30,29	30,30,30	88,86,86	90,89,88	20,16,14	8,7,5	9,7,7	19,16,13	8,7,6	10,9,8	7,6,4	7,5,2	13,10,9	7,6,5	8,6,3	14,11,8

Table 17 The success rate (SR) for the sources in all the test cases in the 2K-SS. The three values in each cell designate the case when no-noise, pink noise of amplitude one and four are considered. 'deep' indicates deep sources, 'int.' indicates intermittent sources and 'shall.' indicates shallow sources

	Mean	Min.	Max.	Detection status	Certainty (0-1)
<i>No noise</i>	3105	4051	1904	30/30	0.9951
<i>pink-1</i>	3857	4998	1846	30/30	0.9613
<i>pink-4</i>	4198	5510	1896	30/30	0.9454

The peak latencies are 100, 400, 500, and 600 ms. The peak widths are 200,100,200, and 400 ms. The peak amplitudes are -1.5, -0.5, 1, and -0.5 μ V.

Table 18 CARSS EVALUATION - 1: The detection of deep sources by CARSS

	Mean	Min.	Max.	Detection status			Certainty (0-1)
				S-I-S-II	S-I/ S-II	None	
<i>No noise</i>	2213	6318	556	18/30	10/30	2/30	0.8585;0.6325
<i>pink-1</i>	2915	7523	1010	16/30	11/30	3/30	0.6644;0.5247
<i>pink-4</i>	3135	7959	254	14/30	12/30	4/30	0.5251; 0.3995

Table 19 CRASS EVALUATION - 2: The detection of deep and near sources by CARSS

The white noise of amplitude 10 % and 40 % of the maximum measurement amplitude is added to the same.

The CARSS identified all the sources and reduced the SS to 6930 out of 15012 in the 5K-SS. The CARSS identified all the sources and reduced the SS to 2843 out of 6012 in the 2K-SS. The sources are identified even under the presence of noise.

The details can be observed from Fig. 6.

Test case-IV:

The dipoles is located at [-69.24, -30.62, -16.12] mm, [-34.91, 18.87, 2.29] mm, [-33.65, 6.60, -17.48], [-35.97, sources and reduced the SS to 3980 out of 15012 in the 7.97, -15.03], [-16.69, -76.23, 39.63] mm, [25.91, 0.68, -5K-SS. The CARSS identified four out of seven sources 39.21] mm and [4.38, -28.65, 77.3] mm oriented along and reduced the SS to 1819 out of 6012 in the 2K-SS. [1,0,0], [0,1,0], [0,0,1], [0,1,0], [1,0,0], [0,1,0] and [0,0,1]The same sources are identified even under the presence are activated. All the seven ERPs are shown in Fig. 7.of noise.

1. Distance from the origin $\|\mathbf{r}_i\|, i = 1$ of S-I is 77.4 mm. Distance between S-I and others $\|\mathbf{r}_{i,j}\|, j = 2 \dots 7$ is 63.0 mm.
2. Distance from the origin $\|\mathbf{r}_i\|, i = 2$ of S-II is 39.8 mm. Distance between S-II and others $\|\mathbf{r}_{i,j}\|, j = 3 \dots 7$ is 23.3 mm.
3. Distance from the origin $\|\mathbf{r}_i\|, i = 3$ of S-III is 38.5 mm. Distance between S-III and others $\|\mathbf{r}_{i,j}\|, j = 4 \dots 7$ is 35.7 mm.
4. Distance from the origin $\|\mathbf{r}_i\|, i = 4$ of S-IV is 39.6 mm. Distance between S-IV and others $\|\mathbf{r}_{i,j}\|, j = 5 \dots 7$ is 75.1 mm.
5. Distance from the origin $\|\mathbf{r}_i\|, i = 5$ of S-V is 87.5 mm. Distance between S-V and others $\|\mathbf{r}_{i,j}\|, j = 6, 7$ is 118.2 mm.
6. Distance from the origin $\|\mathbf{r}_i\|, i = 6$ of S-VI is 47.1 mm. Distance between S-VI and others $\|\mathbf{r}_{i,j}\|, j = 7$ is 122.2 mm.
7. Distance from the origin $\|\mathbf{r}_i\|, i = 7$ of S-VII is 82.6 mm.

The white noise of amplitude 40 % of the maximum measurement amplitude is added to the same.

The CARSS identified only four out of all the sources and reduced the SS to 3980 out of 15012 in the 5K-SS. The CARSS identified four out of seven sources 39.21] mm and [4.38, -28.65, 77.3] mm oriented along and reduced the SS to 1819 out of 6012 in the 2K-SS. [1,0,0], [0,1,0], [0,0,1], [0,1,0], [1,0,0], [0,1,0] and [0,0,1]The same sources are identified even under the presence are activated. All the seven ERPs are shown in Fig. 7.of noise.

S.No.	Noise levels	without CARSS			with CARSS		
		Success Rate	DLE (mm)	SD (mm)	Success Rate	DLE (μ)	SD (mm)
1.	0 dB	30/30	0	11.00 (+12 % to - 2 %)	30/30	0	4.95.00 (+10 % to - 2 %)
2.	pink - 1	30/30	0	29.25 (+21 % to - 8 %)	30/30	0	29.25 (+21 % to - 8 %)
3.	pink - 4	30/30	2.11	40.01(+20 % to - 5 %)	30/30	0	40.01(+20 % to - 5 %)

Table 20 *TEST-CASE (Ext.)-I*:The performance metrics of TRAP-MUSIC when a source is activated.

S.No.	Noise levels	without CARSS			with CARSS		
		Success Rate	DLE (mm)	SD (mm)	Success Rate	DLE (μ)	SD (mm)
1.	0 dB	30/30	0	9.00 (+15 % to - 3 %)	30/30	0	4.66.00 (+11 % to - 2 %)
2.	pink - 1	30/30	0.26	19.95 (+25 % to - 7 %)	30/30	0	12.55 (+32 % to - 9 %)
3.	pink - 4	30/30	4.05	66.51(+10 % to - 15 %)	30/30	0	45.01(+19 % to - 11 %)

Table 21 *TEST-CASE (Ext.)-I*:The performance metrics of Sissy when a source is activated.

S.No.	Noise levels	without CARSS			with CARSS		
		Success Rate	DLE (mm)	SD (mm)	Success Rate	DLE (μ)	SD (mm)
1.	0 dB	22/30	20.56	12.00 (+10 % to - 6 %)	29/30	12.25	6.00 (+10 % to - 10 %)
2.	pink - 1	18/30	45.40	39.50 (+16% to - 10 %)	24/30	22.95	21.24 (+17% to - 12 %)
3.	pink - 4	10/30	52.35	55.95(+29 % to - 20 %)	19/30	39.95	27.56 (+35 % to - 22 %)

Table 22 *TEST-CASE (Ext.)-II*:The performance metrics of Sissy when three deep sources are activated.

The details can be observed from Fig. 7.

6 Discussions

6.1 Monte-carlo simulations

6.1.1 General observations

1. The source localization algorithms performed significantly better with CARSS. The results show the same.
2. Although all the methods localized the active sources correct for one, three, and five sources, they are challenged by the fourth test case where the active sources are seven. The results are evident from the success rates of the active sources in Table. 16 and 17.
3. For the test case-iv alone, the prominence of CARSS in the improvement of the results is not much evident. In the rest of the test cases, CARSS had significantly improved the results.
4. The results in Table. 9 show that not alone deep source localization is more challenging. The neighboring source localization is much more strenuous. The results from Table. 13, 16 and 17 show the same.
5. The sparse bayesian strategy by (Zhang and Rao [2011]) has better estimated the sources than the same by (Wipf et al. [2011]) under the presence of noise.
6. The advantage of ℓ_{21} norm-based method MxNE is visible over the ℓ_2 norm-based methods in estimating the sources.

7. The impotence with ITER's under the presence of noise is very clearly visible in the results.

6.1.2 Case by case observations

Test case-I The A' metric values (Table. 4) show consistency for all the solvers. The ideal value of the A' metric is 1. The number of sources to which CARSS reduced to is presented in Table.1. The number of sources in the SS is reduced by 85 %. The important factor that affects CARSS is the detection of the peak. After detecting the peak, the certainty is calculated. CARSS substantially improved the results.

Test case-II The A' metric values (Table. 5) show consistency for all the solvers. However, slight variations over the first test case are observed (Table. 6). The shallow sources emit prominent scalp distribution that makes their peaks visible at the same location. This is evident in Table. 7. CARSS detected all the sources with the reduction of SS to 25 %.

Test case-III The A' metric values are shown in Table. 6. The test case has two deep sources, an intermittent source, and two shallow sources. All are not near to each other. The spatial extent of the scalp distribution by the shallow sources is dominant but is limited on the scalp. Hence, when two distant shallow sources are active, the interference of peaks does not occur much. The deep sources with a prominent peak on the scalp can be detected by CARSS. This is the reason for CARSS detecting many deep sources in the test case. Also, the presence of shallow sources will attenuate the deep sources. This is a challenge for any solver employed including CARSS. The results are demonstrated in Ta-

S.No.	Noise levels	without CARSS			with CARSS		
		Success Rate	DLE (mm)	SD (mm)	Success Rate	DLE (μ m)	SD (mm)
1.	0 dB	23/30	23.65	8.00 (+14 % to - 4 %)	28/30	9.95	4.70 (+11 % to - 1 %)
2.	pink - 1	19/30	40.40	21.00 (+20% to - 8 %)	25/30	22.50	20.50 (+15% to - 8 %)
3.	pink - 4	10/30	49.55	42.25 (+39 % to - 30 %)	17/30	39.95	35.75 (+26 % to - 13 %)

Table 23 TEST-CASE (Ext.)-II: The performance metrics of TRAP- MUSIC when three deep sources are activated.

S. No.	Test Cases	5K			2K		
		NN	NC-1	NC-2	NN	NC-1	NC-2
1.	TC-1	Y	Y	Y	Y	Y	Y
		1256	1295	1401	875	933	997
2.	TC-2	YYY	YYY	YYY	YYY	YYY	YYY
		4258	4311	4456	1313	1396	1455
3.	TC-3	YYYYY	YYYYY	YYYYY	YYYYY	YYYYY	YYYYY
		6930	7009	7256	2843	2925	3351
4.	TC-4	NNYYYYN	NNYYYYN	NNYYYYN	NNYYYYN	NNYYYYN	NNYYYYN
		3980	4042	1819	1925		

Table 24 Sample test cases: CARSS report for all test cases. The total number of certain sources out of 15,012 (5K) and 6,012 (2K).

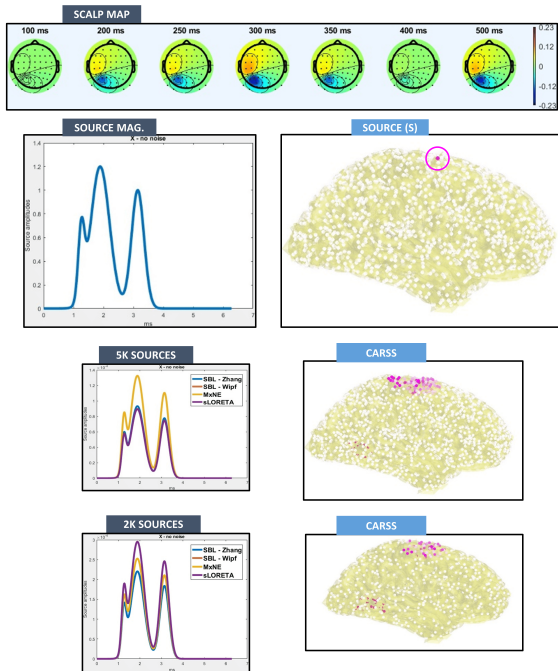


Fig. 4 SAMPLE TEST CASE-I: Scalp maps of the simulated ERP. The peak latencies are 500, 300, and 200 ms. The peak widths are 200, 300 and 100 ms. The peak amplitudes are 1, 1.2, and 0.6μ V. The x-axis represent $t * 2\pi/T, t = 1 \dots 1000, T = 1000$. The ground-truth source activation pattern \mathbf{X} is shown. The reconstructed source magnitude \mathbf{X}^* by the methods in the 2K-SS and 5K-SS are shown. The total number of sources in the 5K-source-space (5K-ss) are 15,012 and in the 2K-source-space (2K-ss) 6,012. CARSS reduced to 875 in 2K-SS and 1256 in 5K-SS when no noise is added.

ble. 16. Three observations for CARSS are - (i) many shallow sources are detected by CARSS. (ii) Many intermediate sources too are detected. (iii) Some deep

sources are missed. Also, some sources are missed due to the interference of scalp distribution. A wrong peak led to detecting the wrong cluster of sources.

Test case-IV: This test case is a challenge for any solver. Seven sources are chosen of which four are near ($Ds(\mathbf{r}_i, \mathbf{r}_j) \leq 55$) deep sources, one intermittent source, and the rest are shallow sources. Enough evidence of source signatures on the scalp is important for any solver to detect. The deep sources are attenuated heavily by the shallow sources. Due to the attenuation, sometimes it may become extremely difficult for any solver to identify. This is what happened in the test case. All the solvers including CARSS are challenged by this test case. The biggest obstacle for CARSS is not the deep sources. It is the near sources that will interfere with each other.

6.1.3 Detailed observations

1. FOCUSS:

1. The general challenges faced by any ITER are: (i) converging to local minima instead of global, (ii) instability under the presence of noise, (iii) Initial estimate dependent and scattering of the solution. They are evident in the results.
2. The instability under the presence of noise can be observed in TC-III (Tables. 9 and 10) and TC-IV (Tables 13 and 10). The localization ability of FOCUSS is challenged a lot under noise although it is better without noise (Table. 17 and 16).
3. FOCUSS had localized the deep sources that are far apart but failed to localize the deep sources that are near. The convergence to the wrong location is observed instead of true in the fourth test case (Tables. 13,14, 17 and 16).

2. MxNE:

1. The trade-off provided by ℓ_{21} norm is evident in the results. The results by MxNE show robustness towards the noise. The success rate of MxNE in localizing sources is higher for MxNE compared to ℓ_2 regularization method (Tables. 16 and 17).
2. The reconstructed sources by MxNE are also sparse.
3. The MxNE couldn't localize many of the four neighboring deep sources clearly (Tables. 16, 17).

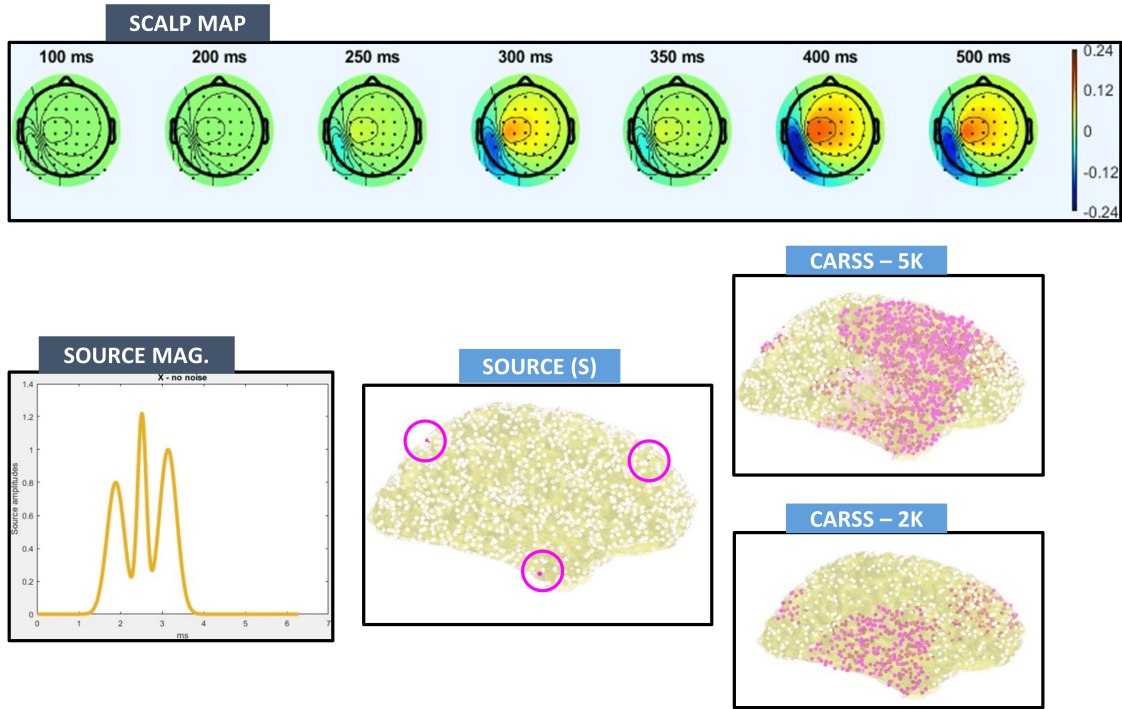


Fig. 5 SAMPLE TEST CASE-II: Scalp maps of the simulated ERP. The peak latencies are 500, 400, and 300 ms. The peak widths are 200, 100 and 200 ms. The peak amplitudes are 1, 1.2, and $0.8 \mu\text{V}$. The ground-truth source activation pattern for all the sources \mathbf{X} is shown. The source is located at $[-39.2764, 42.20, 35.88]$ mm, $[28.77, -74.93, 53.13]$ mm, and $[55.69, -7.10, -41.42]$ mm oriented along $[1,0,0]$, $[0,1,0]$, and $[0,0,1]$. The total number of sources in the 5K-source-space (5K-ss) are 15,012 and in the 2K-source-space (2K-ss) 6,012. CARSS reduced to 4285 in 2K-SS and 1313 in 5K-SS under no noise. The length of the signal is 1000 ms ($T = 1000$). The x-axis represent each sample $t * 2\pi/T, t = 1 \dots 1000, T = 1000$.

3. sLORETA:

1. sLORETA is a well-known ℓ_2 norm regularizer that is simple to implement.
2. The results clearly depict the characteristics of the ℓ_2 norm regularization.
3. Oversmoothing of the solution is observed in many cases. This can be observed in Fig. 6.
4. The ℓ_{21} norm penalization proved better in many aspects compared to ℓ_2 norm regularization.

3. Learning methods:

1. SBL (Wipf et al. [2011]) is accurate but SBL (Zhang and Rao [2013]) is when no noise is present. However, it is complimentary when noise is present. The SBL (Zhang and Rao [2013]) proved to be robust against noise. The results show the same.
2. The SBLs performed much better than FOCUSS. They are fast and efficient than FOCUSS.
3. Both of them failed to localize the three near deep sources in TC-IV.

6.2 CARSS evaluation

1. CARSS can detect deep sources that are far apart. Table. 18. The only issue with the deep sources is the increase in the number of certain sources.
2. The presence of noise shown less impact on the performance of CARSS. The spatial filtering of the measurement vector as suggested in (Michel and Brunet [2019]) is found useful under the presence of noise.
3. The efficacy of CARSS is challenged under multiple neighboring and deep sources. The results are depicted in Table. 19.
4. The effectiveness of CARSS has been limited in TC-IV (Table. 13). The presence of neighboring and deep sources is responsible for the estimation of the wrong cluster as certain sources. Due to this, CARSS had not provided the right SS.

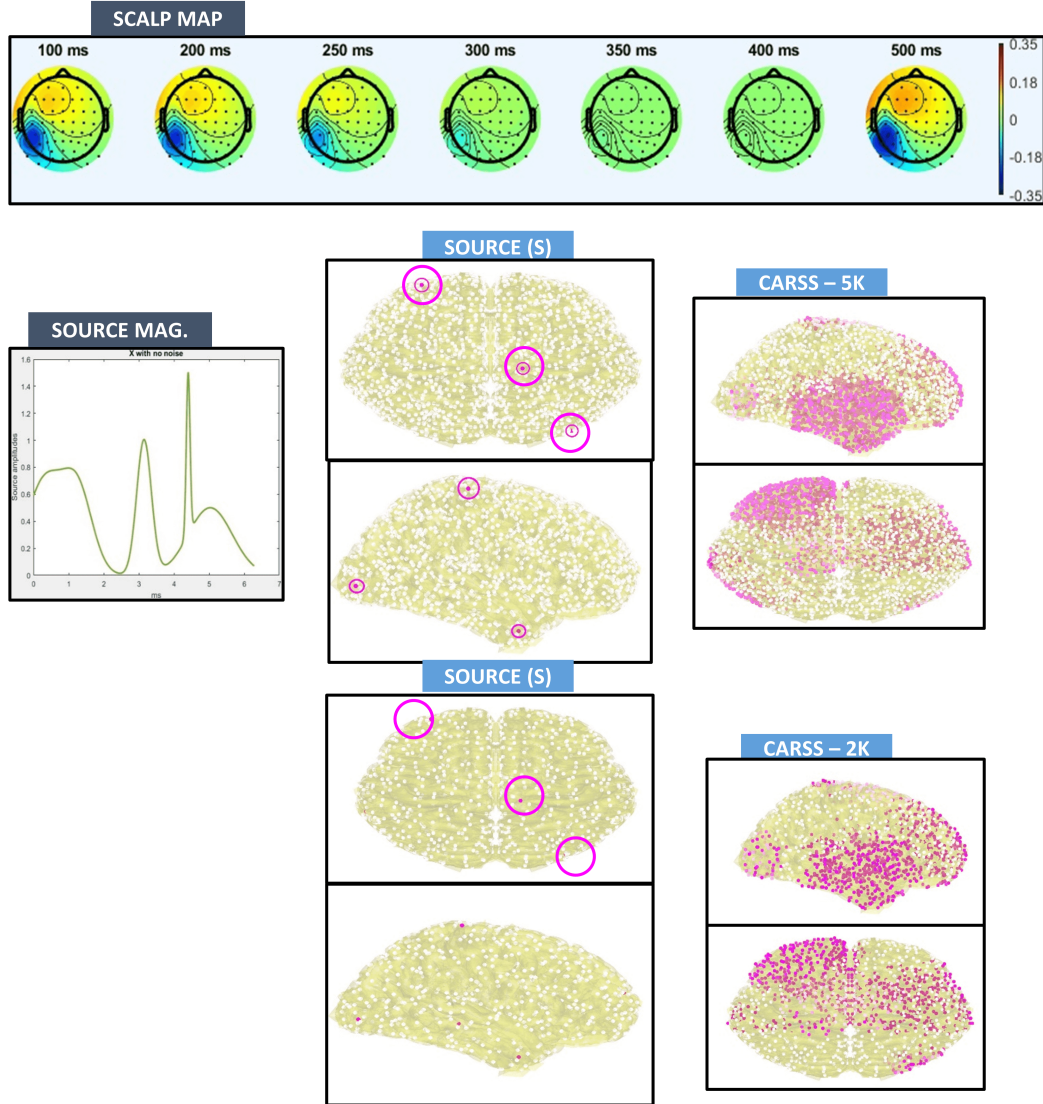


Fig. 6 SAMPLE TEST CASE-III: Scalp maps of the simulated ERP. The peak latencies are 500, 400, and 300 ms. The peak widths are 200, 100 and 200 ms. The peak amplitudes are 1, 1.2, and $0.8 \mu\text{V}$. The ground-truth source activation pattern for all the sources \mathbf{X} is shown. The source is located at $[-35.65, 5.63, 38.84]$ mm, $[-65.19, -39.30, -14.21]$ mm, $[15.45, -27.58, 73.34]$ mm, $[39.05, -73.27, -3.30]$ mm, and $[-32.99, 60.39, 13.64]$ mm oriented along $[1,0,0]$, $[0,1,0]$, $[0,0,1]$, $[0,1,0]$ and $[1,0,0]$. The total number of sources in the 5K-source-space (5K-ss) are 15,012 and in the 2K-source-space (2K-ss) 6,012. CARSS reduced to 4285 in 2K-SS and 1313 in 5K-SS under no noise. The length of the signal is 1000 ms ($T = 1000$). The x-axis represent each sample $t * 2\pi/T, t = 1 \dots 1000, T = 1000$.

6.3 Extended source algorithms

1. The extended source localization algorithms (ESLs) improved significantly with CARSS. The localization accuracy (DLe), and spatial dispersion improved after providing the reduced SS.
2. The ESLs performed exceptionally well under one source activation. There is not much use of CARSS in the test case alone.
3. The presence of deep sources and the presence of noise (in Table. 22 and 23) had affected the performance of ESLs.

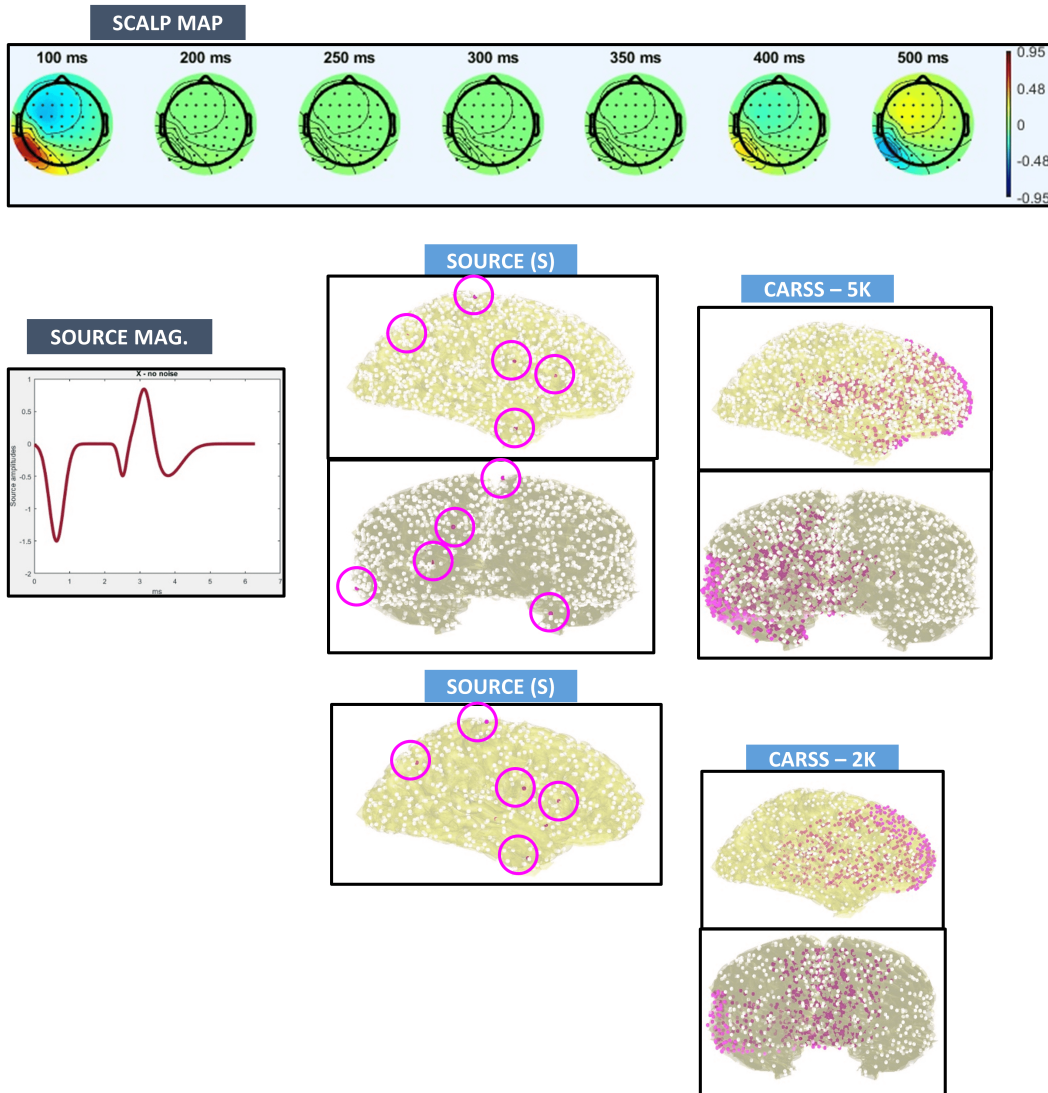


Fig. 7 SAMPLE TEST CASE-IV: Scalp maps of the simulated ERP. The peak latencies are 100, 400, 500, and 600 ms. The peak widths are 200,100,200, and 400 ms. The peak amplitudes are -1.5, -0.5, 1, and -0.5 μ V. The ground-truth source activation pattern for all the sources \mathbf{X} is shown. The source is located at [-69.24, -30.62, -16.12] mm, [-34.91, 18.87, 2.29] mm, [-33.65, 6.60, -17.48], [-35.97, 7.97, -15.03], [-16.69, -76.23, 39.63] mm, [25.91, 0.68, -39.21] mm and [4.38, -28.65, 77.3] mm oriented along [1,0,0], [0,1,0], [0,0,1], [0,1,0], [1,0,0], [0,1,0] and [0,0,1]. The total number of sources in the 5K-source-space (5K-ss) are 15,012 and in the 2K-source-space (2K-ss) 6,012. CARSS reduced to 3980 in 2K-SS and 1819 in 5K-SS under no noise. The length of the signal is 1000 ms ($T = 1000$). The x-axis represent each sample $t * 2\pi/T$, $t = 1 \dots 1000$, $T = 1000$.

6.4 Real data analysis

The solution space reduced by CARSS is presented in Fig. 3. The CSP profile of the sources can be observed. CARSS reduced the solution space to one-thirds at the maximum. MxNE is utilized thereafter. After estimating the source amplitudes, the label powers in the brain are estimated. The atlas followed is the Destrieux atlas

(Destrieux et al. [2010]). There are a total of 148 labels. Then, three labels with maximum power are found out and are presented in Table. 25.

S.No.	Condition	Alcoholic	Control
1.	Single stimuli	G and S cingul Ant R S circular insula ant R S circular insula sup R	S circular insula ant L S circular insula ant R G subcallosal R
2.	Matched	G cingul Post ventral L G precuneus L S occipital ant R	G temp sup G T transv R S occipital ant R G precuneus L
3.	Non-matched	S occipital ant R S circular insula ant R S suborbital L	S suborbital L S circular insula sup R G cingul Post ventral L

Table 25 REAL DATA ANALYSIS: The maximum label powers observed in different experimental conditions. 'cingul' - cingulum; 'ant' - anterior; 'sup' - superior; 'temp' - temporal; 'sup' - superior; 'trans' = transverse; 'G' - gyrus; 'S' - sulcus; 'L' - left; 'R' - right

6.5 Sample tests

After a detailed study of the results, as a summary, some key interpretations eluded regarding CARSS are:

1. The presence of a deep active source increases the number of certain sources. The third test case (Fig. 6) has two deep sources that are identified but the number of certain sources is increased.
2. The presence of many deep sources will also affect the detection of shallow sources. The fourth test case (Fig. 7) has a shallow source unidentified due to the presence of four deep sources.
3. The presence of tangential sources has a more prominent effect than deep sources to be deficient in being picked as a possible candidate. The fourth test case (Fig. 7) has three tangential sources. Tangentially oriented sources may show two approximately equal peaks in the topography that may result in a change of peak locations.
4. The presence of near active sources may mislead and may create a fake cluster of sources. The presence of two near active sources in the fourth test case (Fig. 7) is responsible for the detection of very wrong sources in the CARSS solution space.
5. The spatial filtering of the measurement vector as suggested in (Michel and Brunet [2019]) is found useful under the presence of noise. No much difference in picking the active source and in the number of certain sources under the presence of noise is observed.

The EEG source localization is a challenging problem due to its ill-posedness. The paper presents the current state-of-the-art sparse techniques. The merits and demerits of the solvers are studied. A vast comparative study is performed for eight solvers using a sixty-four channel EEG setup. The MAP solvers, an ℓ_2 norm-based solver, and ℓ_{21} norm-based solver are chosen to compare. CARSS is also tested. some important observations are drawn examining the study.

References

- Sylvain Baillet and Line Garnero. A bayesian approach to introducing anatomo-functional priors in the eeg/meg inverse problem. *IEEE transactions on Biomedical Engineering*, 44(5):374–385, 1997.
- Sylvain Baillet, John C Mosher, and Richard M Leahy. Electromagnetic brain mapping. *IEEE Signal processing magazine*, 18(6):14–30, 2001.
- Hanna Becker, Pierre Comon, Laurent Albera, Martin Haardt, and Isabelle Merlet. Multi-way space–time–wave-vector analysis for eeg source separation. *Signal Processing*, 92(4):1021–1031, 2012.
- Hanna Becker, Laurent Albera, Pierre Comon, Martin Haardt, Gwénaél Birot, Fabrice Wendling, Martine Gavaret, Christian-George Bénar, and Isabelle Merlet. Eeg extended source localization: tensor-based vs. conventional methods. *NeuroImage*, 96:143–157, 2014.
- Hanna Becker, Laurent Albera, Pierre Comon, J-C Nunes, Rémi Gribonval, Julien Fleureau, Philippe Guillotel, and Isabelle Merlet. Sissy: An efficient and automatic algorithm for the analysis of eeg sources based on structured sparsity. *NeuroImage*, 157:157–172, 2017.
- Gwénaél Birot, Laurent Albera, Fabrice Wendling, and Isabelle Merlet. Localization of extended brain sources from eeg/meg: the exso-music approach. *NeuroImage*, 56(1):102–113, 2011.
- Shane F Cotter, Bhaskar D Rao, Kjersti Engan, and Kenneth Kreutz-Delgado. Sparse solutions to linear inverse problems with multiple measurement vectors. *IEEE Transactions on Signal Processing*, 53(7):2477–2488, 2005.
- Anders M Dale and Martin I Sereno. Improved localization of cortical activity by combining eeg and meg with mri cortical surface reconstruction: a linear approach. *Journal of cognitive neuroscience*, 5(2):162–176, 1993.
- Felix Darvas, D Pantazis, E Kucukaltun-Yildirim, and RM Leahy. Mapping human brain function with meg and eeg: methods and validation. *NeuroImage*, 23:S289–S299, 2004.
- Christophe Destrieux, Bruce Fischl, Anders Dale, and Eric Halgren. Automatic parcellation of human cortical gyri and sulci using standard anatomical nomenclature. *Neuroimage*, 53(1):1–15, 2010.
- Lei Ding. Reconstructing cortical current density by exploring sparseness in the transform domain. *Physics in Medicine & Biology*, 54(9):2683, 2009.
- Karl Friston. Hierarchical models in the brain. *PLoS computational biology*, 4(11):e1000211, 2008.

- Karl Friston, Lee Harrison, Jean Daunizeau, Stefan Kiebel, Christophe Phillips, Nelson Trujillo-Barreto, Richard Henson, Guillaume Flandin, and Jérémie Mattout. Multiple sparse priors for the m/eeg inverse problem. *NeuroImage*, 39(3):1104–1120, 2008.
- Karl J Friston, William Penny, Christophe Phillips, S Kiebel, G Hinton, and John Ashburner. Classical and bayesian inference in neuroimaging: theory. *NeuroImage*, 16(2):465–483, 2002.
- Sónia I Gonçalves, Jan C de Munck, Jeroen PA Verbunt, Fetsje Bijma, Rob M Heethaar, and F Lopes da Silva. In vivo measurement of the brain and skull resistivities using an eit-based method and realistic models for the head. *IEEE Transactions on Biomedical Engineering*, 50(6):754–767, 2003.
- Irina F Gorodnitsky and Bhaskar D Rao. Sparse signal reconstruction from limited data using focuss: A re-weighted minimum norm algorithm. *IEEE Transactions on signal processing*, 45(3):600–616, 1997.
- Irina F Gorodnitsky, John S George, and Bhaskar D Rao. Neuromagnetic source imaging with focuss: a recursive weighted minimum norm algorithm. *Electroencephalography and clinical Neurophysiology*, 95(4):231–251, 1995.
- Alexandre Gramfort. *Mapping, timing and tracking cortical activations with MEG and EEG: Methods and application to human vision*. PhD thesis, 2009.
- Alexandre Gramfort, Matthieu Kowalski, and Matti Hämäläinen. Mixed-norm estimates for the m/eeg inverse problem using accelerated gradient methods. *Physics in medicine and biology*, 57(7):1937, 2012.
- Alexandre Gramfort, Daniel Strohmeier, Jens Haueisen, Matti S Hämäläinen, and Matthieu Kowalski. Time-frequency mixed-norm estimates: Sparse m/eeg imaging with non-stationary source activations. *NeuroImage*, 70:410–422, 2013.
- Alexandre Gramfort, Martin Luessi, Eric Larson, Denis A Engemann, Daniel Strohmeier, Christian Brodbeck, Lauri Parkkonen, and Matti S Hämäläinen. Mne software for processing meg and eeg data. *Neuroimage*, 86:446–460, 2014.
- Roberta Grech, Tracey Cassar, Joseph Muscat, Kenneth P Camilleri, Simon G Fabri, Michalis Zervakis, Petros Xanthopoulos, Vangelis Sakkalis, and Bart Vanrumste. Review on solving the inverse problem in eeg source analysis. *Journal of neuroengineering and rehabilitation*, 5(1):25, 2008.
- Hans Hallez, Bart Vanrumste, Roberta Grech, Joseph Muscat, Wim De Clercq, Anneleen Vergult, Yves D’Asseler, Kenneth P Camilleri, Simon G Fabri, Sabine Van Huffel, et al. Review on solving the forward problem in eeg source analysis. *Journal of neuroengineering and rehabilitation*, 4(1):46, 2007.
- Matti S Hämäläinen and Risto J Ilmoniemi. *Interpreting measured magnetic fields of the brain: estimates of current distributions*. Helsinki University of Technology, Department of Technical Physics, 1984.
- Per Christian Hansen and Dianne Prost O’Leary. The use of the l-curve in the regularization of discrete ill-posed problems. *SIAM Journal on Scientific Computing*, 14(6):1487–1503, 1993.
- Stefan Haufe and Arne Ewald. A simulation framework for benchmarking eeg-based brain connectivity estimation methodologies. *Brain topography*, 32(4):625–642, 2019.
- Stefan Haufe, Vadim V Nikulin, Klaus-Robert Müller, and Guido Nolte. A critical assessment of connectivity measures for eeg data: a simulation study. *Neuroimage*, 64:120–133, 2013.
- Ming-Xiong Huang, Anders M Dale, Tao Song, Eric Halgren, Deborah L Harrington, Igor Podgorny, Jose M Canive, Stephen Lewis, and Roland R Lee. Vector-based spatial-temporal minimum l1-norm solution for meg. *NeuroImage*, 31(3):1025–1037, 2006.
- Yu Huang, Lucas C Parra, and Stefan Haufe. The new york head—a precise standardized volume conductor model for eeg source localization and tes targeting. *NeuroImage*, 140:150–162, 2016.
- Lester Ingber. Statistical mechanics of neocortical interactions: Canonical momenta indicators of electroencephalography. *Physical Review E*, 55(4):4578, 1997.
- Lester Ingber. Statistical mechanics of neocortical interactions: Training and testing canonical momenta indicators of eeg. *Mathematical and computer modelling*, 27(3):33–64, 1998.
- Tamara G Kolda and Brett W Bader. Tensor decompositions and applications. *SIAM review*, 51(3):455–500, 2009.
- Laurens R Krol, Juliane Pawlitzki, Fabien Lotte, Klaus Gramann, and Thorsten O Zander. Sereega: Simulating event-related eeg activity. *Journal of neuroscience methods*, 309:13–24, 2018.
- Tulaya Limpiti, Barry D Van Veen, and Ronald T Wakai. Cortical patch basis model for spatially extended neural activity. *IEEE Transactions on Biomedical Engineering*, 53(9):1740–1754, 2006.
- Hesheng Liu and Paul H Schimpf. Efficient localization of synchronous eeg source activities using a modified rap-music algorithm. *IEEE transactions on biomedical engineering*, 53(4):652–661, 2006.
- Niko Mäkelä, Matti Stenroos, Jukka Sarvas, and Risto J Ilmoniemi. Truncated rap-music (trap-music) for meg and eeg source localization. *NeuroImage*, 167:73–83, 2018.

- Teja Manneppalli and Aurobinda Routray. Certainty-based reduced sparse solution for dense array eeg source localization. *IEEE Transactions on Neural Systems and Rehabilitation Engineering*, 27(2):172–178, 2019.
- Kanta Matsuura and Yoichi Okabe. Selective minimum-norm solution of the biomagnetic inverse problem. *IEEE Transactions on Biomedical Engineering*, 42(6):608–615, 1995.
- Christoph M Michel and Denis Brunet. Eeg source imaging: a practical review of the analysis steps. *Frontiers in neurology*, 10:325, 2019.
- Christoph M Michel and Micah M Murray. Towards the utilization of eeg as a brain imaging tool. *Neuroimage*, 61(2):371–385, 2012.
- Christoph M Michel, Micah M Murray, Göran Lantz, Sara Gonzalez, Laurent Spinelli, and Rolando Grave de Peralta. Eeg source imaging. *Clinical neurophysiology*, 115(10):2195–2222, 2004.
- Christoph M Michel, Thomas Koenig, Daniel Brandeis, Jiří Wackermann, and Lorena RR Gianotti. *Electrical neuroimaging*. Cambridge University Press, 2009.
- A Molins, Steven M Stufflebeam, Emery N Brown, and Matti S Hämäläinen. Quantification of the benefit from integrating meg and eeg data in minimum l2-norm estimation. *Neuroimage*, 42(3):1069–1077, 2008.
- John C Mosher and Richard M Leahy. Source localization using recursively applied and projected (rap) music. *IEEE Transactions on signal processing*, 47(2):332–340, 1999.
- John C Mosher, Sylvain Baillet, Felix Darvas, Dimitrios Pantazis, E Yildirim, and R Leahy. Brainstorm electromagnetic imaging software. In *5th International Symposium on Noninvasive Functional Source Imaging within the Human Brain and Heart (NFSI 2005)*, 2005.
- Micah M Murray, Denis Brunet, and Christoph M Michel. Topographic erp analyses: a step-by-step tutorial review. *Brain topography*, 20(4):249–264, 2008.
- J. Nolte and J.W. Sundsten. *The Human Brain: An Introduction to Its Functional Anatomy*. Mosby/Elsevier, 2009.
- Paul L Nunez, Ramesh Srinivasan, et al. *Electric fields of the brain: the neurophysics of EEG*. Oxford University Press, USA, 2006.
- Vangelis P Oikonomou and Ioannis Kompatsiaris. A novel bayesian approach for eeg source localization. *Computational Intelligence and Neuroscience*, 2020, 2020.
- Robert Oostenveld, Pascal Fries, Eric Maris, and Jan-Mathijs Schoffelen. Fieldtrip: open source software for advanced analysis of meg, eeg, and invasive electrophysiological data. *Computational intelligence and neuroscience*, 2011:1, 2011.
- Wanmei Ou, Matti S Hämäläinen, and Polina Golland. A distributed spatio-temporal eeg/meg inverse solver. *NeuroImage*, 44(3):932–946, 2009.
- Roberto D Pascual-Marqui, Christoph M Michel, and Dietrich Lehmann. Low resolution electromagnetic tomography: a new method for localizing electrical activity in the brain. *International Journal of psychophysiology*, 18(1):49–65, 1994.
- Roberto Domingo Pascual-Marqui et al. Standardized low-resolution brain electromagnetic tomography (sloreta): technical details. *Methods Find Exp Clin Pharmacol*, 24(Suppl D):5–12, 2002.
- Saeid Sanei and Jonathon A Chambers. *EEG signal processing*. John Wiley & Sons, 2013.
- Ralph Schmidt. Multiple emitter location and signal parameter estimation. *IEEE transactions on antennas and propagation*, 34(3):276–280, 1986.
- Joan G Snodgrass and Mary Vanderwart. A standardized set of 260 pictures: norms for name agreement, image agreement, familiarity, and visual complexity. *Journal of experimental psychology: Human learning and memory*, 6(2):174, 1980.
- Daniel Strohmeier, Yousra Bekhti, Jens Haueisen, and Alexandre Gramfort. The iterative reweighted mixed-norm estimate for spatio-temporal meg/eeg source reconstruction. *IEEE transactions on medical imaging*, 35(10):2218–2228, 2016.
- Robert Tibshirani, Michael Saunders, Saharon Rosset, Ji Zhu, and Keith Knight. Sparsity and smoothness via the fused lasso. *Journal of the Royal Statistical Society: Series B (Statistical Methodology)*, 67(1):91–108, 2005.
- Luc Vincent and Pierre Soille. Watersheds in digital spaces: an efficient algorithm based on immersion simulations. *IEEE Transactions on Pattern Analysis & Machine Intelligence*, 13(06):583–598, 1991.
- David Wipf and Srikantan Nagarajan. A unified bayesian framework for meg/eeg source imaging. *NeuroImage*, 44(3):947–966, 2009.
- David P Wipf and Bhaskar D Rao. An empirical bayesian strategy for solving the simultaneous sparse approximation problem. *IEEE Transactions on Signal Processing*, 55(7):3704–3716, 2007.
- David P Wipf, Julia P Owen, Hagai T Attias, Kensuke Sekihara, and Srikantan S Nagarajan. Robust bayesian estimation of the location, orientation, and time course of multiple correlated neural sources using meg. *NeuroImage*, 49(1):641–655, 2010.
- David P Wipf, Bhaskar D Rao, and Srikantan Nagarajan. Latent variable bayesian models for promoting sparsity. *IEEE Transactions on Information Theory*,

57(9):6236–6255, 2011.

David Paul Wipf. *Bayesian methods for finding sparse representations*. PhD thesis, UC San Diego, 2006.

Peng Xu, Yin Tian, Huafu Chen, and Dezhong Yao. Lp norm iterative sparse solution for eeg source localization. *IEEE transactions on biomedical engineering*, 54(3):400–409, 2007.

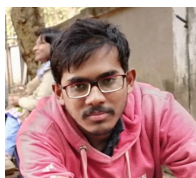
Jun Yao and Julius PA Dewald. Evaluation of different cortical source localization methods using simulated and experimental eeg data. *Neuroimage*, 25(2):369–382, 2005.

De-xiang Zhang, Xiao-pei Wu, and Xiao-jing Guo. The eeg signal preprocessing based on empirical mode decomposition. In *Bioinformatics and Biomedical Engineering, 2008. ICBBE 2008. The 2nd International Conference on*, pages 2131–2134. IEEE, 2008.

Zhilin Zhang and Bhaskar D Rao. Sparse signal recovery with temporally correlated source vectors using sparse bayesian learning. *IEEE Journal of Selected Topics in Signal Processing*, 5(5):912–926, 2011.

Zhilin Zhang and Bhaskar D Rao. Extension of sbl algorithms for the recovery of block sparse signals with intra-block correlation. *IEEE Transactions on Signal Processing*, 61(8):2009–2015, 2013.

Min Zhu, Wenbo Zhang, Deanna L Dickens, and Lei Ding. Reconstructing spatially extended brain sources via enforcing multiple transform sparseness. *NeuroImage*, 86:280–293, 2014.



Teja Mannepalli is born in Chirala, Andhra Pradesh, India, on 13th April 1994. He received his B.Tech. degree in Electrical engineering, in 2015 and M.Tech. in Instrumentation and signal processing in 2016 from Indian Institute of Technology, Kharagpur. He is currently a research scholar from IIT

Kharagpur working towards Ph.D. His known areas are signal processing, biomedical instrumentation, and linear algebra.



Aurobinda Routray is born on March 31, 1965. He received the B.Sc. Eng. from National Institute of Technology, Rourkela, India, M. Tech from, Indian Institute of Technology, Kanpur, India, and Ph. D from Sambalpur University, Odisha, India in 1989, 1991, and 1999 respectively.

He is currently the Associate Dean, Infrastructure (Electrical), in IIT Kharagpur, India. He is associated with the Department of Electrical Engineering as a Professor. He won Samsung GRO Award in 2012 and

State Young Scientist Award in 1999. His research interests include biomedical, statistical signal processing, and embedded systems. He is a member of the IEEE.